DEVELOPMENT OF PROSPECTIVE GATING IN STATIONARY DIGITAL CHEST TOMOSYNTHESIS USING A CARBON NANOTUBE X-RAY SOURCE ARRAY

Allison Etta Hartman

A dissertation submitted to the faculty of the University of North Carolina at Chapel Hill in partial fulfillment of the requirements for the degree of Doctor of Philosophy in the Department of Physics.

Chapel Hill
2017

Approved by:

Tamara Branca

Hugon Karwowski

David Lalush

Yueh Lee

Jianping Lu

Otto Zhou

ABSTRACT

Allison Etta Hartman: Development of prospective gating in stationary digital chest tomosynthesis using a carbon nanotube x-ray source array
(Under the direction Otto Zhou)

Purpose: To quantify the benefit of prospectively gated stationary digital chest tomosynthesis (Gs-DCT) using a carbon nanotube (CNT) x-ray source array in a free breathing porcine study.

Methods: The Gs-DCT x-ray system consists of a linear x-ray array tube (80kVp, 0.125mAs per projection for 29 projections over a 12° angular span) and a flat panel detector (5 fps). Imaging was performed on an anesthetized, free-breathing 13.5kg pig. A respiratory trace was acquired through a transducer belt around the thorax. Each gated projection image was acquired at the temporal coincidence of the detector integration time and the peak inhalation of the pig. The projection images were reconstructed using iterative reconstruction with a 2mm slice thickness using iterative reconstruction. Image blur was assessed as the reproduction of the diaphragm in the reconstructed images. Respiratory phase timing quality was assessed through cross-correlation analysis.

Results: Animal respiration rate was 24.3±3.5bpm. The scan time for the gated scan was 86.9s±2.9s compared to the un-gated scanning time 6.3 ±.6s. An entrance dose of 0.4mSv was used. The blur in the reproduction of the diaphragm in the reconstructed images for gated study was 1.8± 0.5mm where in the un-gated case the diaphragm was 2.6±0.6 mm. The average cross correlation coefficient between of the respiratory trace at the time of the x-ray pulse was .91±.02 for the gated scan and .11±.01 for the un-gated scan.

Conclusions: Prospective gated imaging significantly reduced the motion blur, substantially improving the image quality of the tomosynthesis images. The CNT based x-ray sources enable precise x-ray pulse generation on demand. If enabled clinically, the Gs-DCT system could potentially obtain 3D image stacks in patients that are unable to hold their breaths, such as the pediatric or intubated patient population. Prospectively gated human studies are planned.

To my Zady

ACKNOWLEDGEMENTS

First and foremost, I would like to thank Dr. Hugon Karwowski for his advice, guidance, and encouragement throughout this project. I am greatly appreciative to my dissertation advisor, Dr. Zhou. I am thankful to Dr. Lee for making me more resilient and to Dr. Lu for helping me develop new ideas to solve problems. I appreciate Dr. David Lalush and Dr. Tamara Branca for serving on my committee and asking insightful questions throughout meetings and presentations. I would like to thank past and present group members including Taylor Gunnel, Connor Puett, Jabari Calliste, Pavel Chtcheprove, Christy Inscoe, Gongting Wu, Lei Zhang, Jing Shan, and Soha Bazyar for their camaraderie and support.

I would like to thank the amazing educators at the Northfield Mount Hermon School. I would not be here without the patience of Jeanne Reese and the dorm leaders of Mackinnon. I am thankful for the support of my amazing family throughout my education. I would like to thank my Bubby, Janet Hartman, for always believing in me. I am thankful to my Granddad for supporting me through the College of the Holy Cross and for pushing me to be a better person. I am thankful to my Auntie Mardie Hinkley fostering a love of learning in me and for being a great role model. I am grateful to my Auntie Mary Blanchette for all of her great advice throughout graduate school.

I am grateful for my physics cohort, including Rohan Isaac and Jamin Rager, for so many fun times and for keeping me sane. I am thankful to Jessie Barrack, Ana Doblas, Ben Muñoz, Gulfo and Luke for their constant love and support.

I am extremely grateful to my parents who gave me the best education they could find and for being so supportive of my crazy endeavors.

Most of all, I am thankful for the constant love, support, and patience from Scott Ravyts. I would not be the person I am today without you.

TABLE OF CONTENTS

LIST OF TABLES

LIST OF FIGURES

LIST OF ABBREVIATIONS

AFS	Artifact spread function
AFVR	Adapted fan-beam volume reconstruction
AWT	Acquisition window true
AP	Anterior-posterior
BMI	Body mass index
BPM	breaths or beats per minute
BRIC	Biomedical research imaging center
BT	Buffer time
CF	Cystic Fibrosis
CNR	Contrast to noise ratio
CNT	Carbon nanotube
CT	Computed tomography
CXR	Chest x-ray radiography
DAQ	Data acquisition board
DCT	Digital chest tomosynthesis
DSCT	Dual-source computed tomography
ECG	electrocardiogram
FDA	Food and drug administration
FPS	Frames per second
FWHM	Full width half max
GPIB	General purpose interface bus
LCA	Lateral costophrenic angles
LN	Lung nodule
LSF	Line spread function
Micro-CT	Micro-computed tomography
MPE	Multi pixel electronics
MRT	Micro beam radiation therapy
MTF	Modulation transfer function

PA	Posterior-anterior
PVDR	Peak valley dose ratio
PW	Pulse width
ROI	Region of interest
s-DBT	Stationary digital breast tomosynthesis
s-DCT	Stationary digital chest tomosynthesis
SID	Source to detector distance
SOD	Source to object distance
SIRT	Simultaneous iterative reconstruction technique
SNR	Signal to noise ratio
TTL	Transistor-transistor logic
UNC	University of North Carolina at Chapel Hill

CHAPTER 1
Introduction

1.1 Overview

Patients with lung disease are normally monitored with a 2D chest radiograph (CXR). CXR uses a relatively low radiation dose and is low cost. The sensitivity of a radiograph is relatively poor due to the superposition of normal anatomy over lesions. Studies have shown poor lung nodule sensitivity for lesions less than 10mm. (Vult von Steyern et al., 2012; Dobbins et al., 2008b; Terzi et al., 2013b) If there are suspicious indications on the CXR image, a computed tomography (CT) scan can be required. A CT scan is the gold standard for chest imaging but requires a large dose of radiation and is a high cost to the patient. In order to address these limitations, digital chest tomosynthesis (DCT) has been developed.

DCT is an imaging modality that uses X-ray projection images acquired over a limited scanning angle to reconstruct a 3D image of the lung field. The projection images are taken by translating a conventional X-ray source. The projection images are reconstructed into a sequence of tomosynthesis slices, each showing a different depth. The effects of overlapping tissues are minimized in tomosynthesis imaging thus providing increased contrast of anatomic structures and depth localization of lesions. This technology has been clinically used for breast and chest imaging.(Good et al., 2008; Sechopoulos, 2013; Dobbins et al., 2008a) DCT has been shown to have better sensitivity than CXR.(Dobbins et al., 2008b) DCT clinical trials have shown that tomosynthesis can detect nodules as small as 5mm.(Dobbins and Mcadams, 2009; Vikgren et al., 2008; Bertolaccini et al., 2015) The American College of Radiology has released a LungRADS assessment chart for the standardization of lung nodule screening. The LungRADS assessment chart recommends a 1 year follow-up for nodules less than 6mm.(Rad, 2014) Therefore, DCT screening could have the potential to reduce the need for CT scans.

One main limitation of DCT is the long scan time. The scanning time is limited by the mechanical motion of the X-ray source. A conventional X-ray source uses a metal filament (cathode), which is heated to emit electrons that are accelerated to strike a metal target (anode) to create X-rays. Conventional X-ray tubes emit X-rays from a single focal spot. Our research group has developed a field emission X-ray source array technology using carbon nanotubes (CNTs) as the cold cathode.(Cheng and Zhou, 2003) A stationary digital breast tomosynthesis (s-DBT) using a CNT X-ray source array has been successfully developed and installed in the University of North Carolina Womens Hospital for clinical trials.(Tucker et al., 2014; Wu et al., 2015; Qian et al., 2012) Using the X-ray source array, the stationary digital chest tomosynthesis (s-DCT) system can achieve full angular coverage in tomosynthesis imaging with no moving parts. Previous studies on the stability and geometry of the s-DCT system have been published.(Shan et al., 2013, 2014a)

The goal of this project was to develop prospective gating in stationary digital chest tomosynthesis using a carbon nanotube X-ray source array in order to increase image quality for patients who cannot complete a breath hold for lung imaging.

1.2 Specific research aims

1.2.1 Research Aim 1

The first research aim was to convert the bench top tomosynthesis system into a clinical prototype s-DCT system. This required moving the equipment to a research imaging center, making the system electrical safety and radiation safety compliant, and imaging patients to evaluate the diagnostic relevance of s-DCT.

1.2.2 Research Aim 2

The second research aim was to create the gated stationary digital chest tomosynthesis (Gs-DCT) system. This required integrating a flat panel detector, CNT X-ray source, and frame grabber card. Customized operating software was developed to trigger and save the X-ray images. The system was then electrical and radiation safety certified.

1.2.3 Research Aim 3

The final research aim was to quantify the benefit of the Gs-DCT system. The system was fully characterized and tested in two porcine studies. The main research questions were: Is the temporal resolution of this system high enough to image in-vivo animals, will global patient motion blur overpower the benefit of gating, and will gating yield diagnostically relevant images?

1.3 Dissertation organization

This dissertation is organized in the following order: Chapter two focuses on the background of X-ray imaging for medical purposes and gated imaging. The first part of chapter two covers X-ray generation, image formation and quality assessment. The second part of chapter two covers key factors in gating and current applications of gating. Chapter three covers the work completed on Aim 1 of this dissertation including previous the work done on the clinical prototype of the s-DCT system, including the materials and methods of the X-ray source, the dosimetry used, and the patient studies completed using this system. Chapter four reviews the work completed on Aim 2 and details the application of gated imaging to the s-DCT. Chapter five covers the work completed on Aim 3 and quantify the benefit of the Gs-DCT system. Chapter six includes conclusions of this dissertation and proposed future work for the Gs-DCT system.

CHAPTER 2
X-ray imaging for medical purposes

2.1 Introduction

This chapter covers key components of X-ray imaging and applications. X-ray imaging is the most widely used medical test. The images allow physicians to gain anatomic and functional information non-invasively. This chapter first explains conventional X-ray generation. Conventional X-ray sources are used in all commercial transmission X-ray based imaging systems but have limitations that are discussed here. To address the limitations of a conventional X-ray source, a carbon nanotube (CNT) X-ray source has been invented. The second section of this chapter discusses the CNT X-ray source and its applications. The third section of this chapter gives a short overview of image formation and the ways image quality is assessed; image quality parameters will be analyzed in later chapters. The last section of this chapter provides a background to gated imaging including key factors in gating and current applications for gating.

2.2 Conventional X-ray generation

X-rays are generated by taking energy from electrons and converting it into photons. X-ray tubes are used for all transmission X-ray imaging. There are two main parts to the X-ray tube. The first is the energetic electron supplier. In a conventional X-ray source, a large current is passed through a metal filament, due to the resistance, the filament is heated. When the filament temperature is high enough, electrons are ejected from the metal through thermal emission. The source of the electrons is known as the cathode and is commonly tungsten. A schematic of a conventional X-ray source is shown in figure 2.1.

The second part of an X-ray tube is the positively biased target, where the electron energy is converted into photons, this is known as the anode. The X-rays are created when the electrons are focused and bombard the anode at the focal spot. The intensity of the X-rays is directly proportional

to the current of the electrons generated by the cathode and by the square of the voltage applied to the anode. The anode is normally a heavy metal, such as tungsten. This type of X-ray source is known as a thermionic source. The emission of electron is dependent on the thermal energy of the electron to break the potential barrier between the cathode and vacuum.

There are two main processes that occur when the electrons hit the metal target. The first process is Bremsstrahlung radiation, produced by the slowing of the electrons hitting the metal target. Bremsstrahlung radiation produces a continuous distribution of X-ray energies and is the primary process for chest imaging radiation. The second process produces characteristic X-rays. Characteristic X-rays are generated when the bombarding electrons have enough energy to knock an electron out of one of the inner shells of the target metal atoms. Then the electrons from higher shells drop down to fill the vacancy, emitting X-ray photons with precise energies determined by electron energy levels. Characteristic X-rays are formed anytime the incoming electrons have an energy above the K-edge of the metal target. For mammography, the bremsstrahlung radiation is filtered out and only the characteristic X-rays are used. This allows for more accurate attenuation measurements in the images. For chest imaging, there is not enough characteristic X-rays to effectively image the chest. Therefore, Bremsstrahlung radiation is the dominant source of spectra seen for the systems analyzed here.

The amount of radiation an X-ray source emits in a given time is known as the X-ray flux. The higher the current emitted from the cathode, the higher X-ray flux that is output from the X-ray tube. A large X-ray flux will decrease the amount of 'beam-on' time needed to deposit a given amount of dose on the detector.

2.2.1 Bremsstrahlung radiation

Modern diagnostic X-ray generation is a product of the deceleration of electrons, usually electrons, when they are slowed down by the anode. The energy of the radiated photon is equal to the loss of kinetic energy of the electrons. The energy output from Bremsstrahlung radiation is continuous with the maximum energy equal to the input energy of the charge carrier. There are fewer photons near the maximum photon energy because there is a low probability of complete transfer of electron kinetic energy to photon energy. The energy spectra from Bremsstrahlung radiation can be seen in figure 2.2.

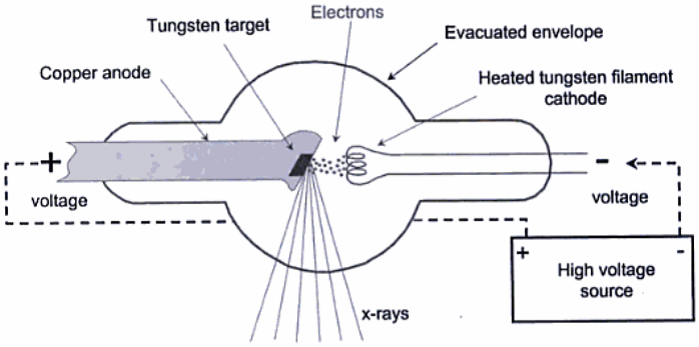

Figure 2.1: A schematic of a conventional X-ray tube. The right hand side shows the heated tungsten filament emitting electrons towards the anode. (Bushberg, Jerrold T. , Seibert, J. Anthony, Leidholdt, Edwin Jr, Boone, 2002)

The low energy photons do not have enough energy to pass through the patient without scattering. Therefore, they do not add to the image quality. These photons add more X-ray dose to the patient because they have a higher probability of being absorbed in the body and are ionizing radiation that cause harm to cells. According to the food and drug administration (FDA) standards, X-ray sources require filtration to be used to prevent unnecessary X-ray dose the the patient. The spectra in figure 2.2 corresponds to the the anode voltage at 90kVp with a low energy filter to prevent unnecessary radiation exposure to the patient.

2.2.2 Limitations of conventional X-ray sources

Only 1% of the primary energy of the X-ray source is converted into bremsstrahlung radiation in a conventional X-ray tube. (Behlig, 2016; Oppelt, 2005) Most energy is lost due to the back scattering of electrons and heat dispersion. 50% of the primary electrons are backscattered from the anode and do not create X-rays. (Behlig, 2016; Oppelt, 2005) This inefficiency causes several limitations to the X-ray source.

For 3D imaging, the X-ray source must illuminate the detector from multiple angles. With a conventional single source X-ray system, that would require motion of the X-ray source and/or detector to acquire images. In order to address this concern, for many 3D imaging applications, the detector and X-ray source are mounted to a rotating gantry. It is impractical to put conventional X-ray sources close together because of the large size and increased cost. (Neculaes et al., 2014a)

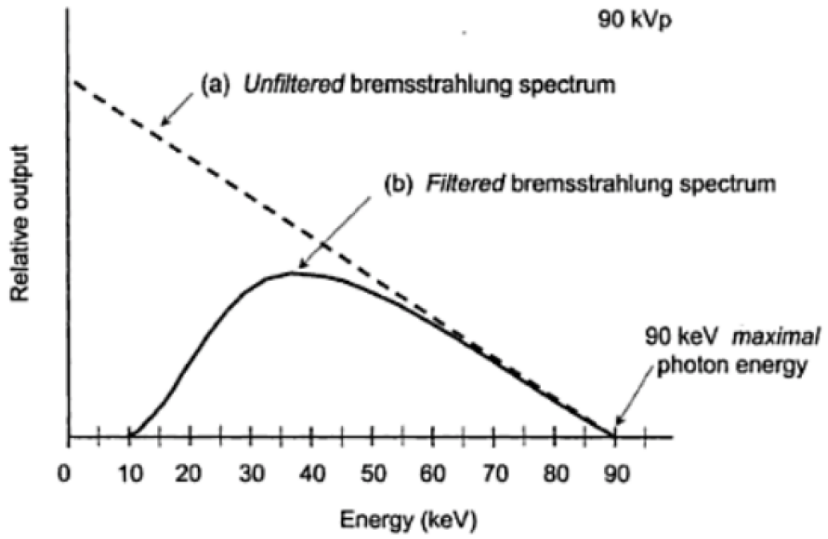

Figure 2.2: This spectra shows the probability of each energy being output from the X-ray source due to Bremsstrahlung radiation with a low energy filter such as aluminum. (Bushberg, Jerrold T. , Seibert, J. Anthony, Leidholdt, Edwin Jr, Boone, 2002)

High operating temperature and power consumption are some major limitation of a conventional X-ray source. The flux of the X-ray source is largely constrained by the heat dissipation of the anode. One solution is to rotate the anode during imaging. The rotation of the anode spreads the heat load over a much larger volume than a stationary anode. An oil cooling system can also be implemented to dissipate heat away from the anode. The cooling system for the anode, increases the size of the system. The power consumption for a conventional X-ray source is high because the inefficiency of the cathode. (Kandlakunta et al., 2017)

Electron-beam CT was invented to complete a CT scan with no mechanical motion.(Neculaes et al., 2014a) In a electron-beam scanner, an electron gun creates an electron beam aimed at a target rings. This creates the effect of hanging a continuous X-ray source around the patient. These target rings produce the X-rays and a detector ring collects the images. One main application of this system is cardiac calcium scoring. However, a major challenge of the electron-beam CT is the small scanning volume. There is little collimation for each X-ray source which creates challenges in localizing the detector location with respect to the source. (Neculaes et al., 2014b)

Another limitation of the thermionic sources is the poor temporal resolution of the cathode. Due to the high temperatures needed, thermionic emission cannot be switched rapidly. In order to increase temporal resolution, external mechanical shuttering needs to be implemented. In general,

this leads to poor response time, difficulty generating uniform, and non-periodic X-ray pulses. Both of these qualities are needed for gated imaging of moving objects. In addition, the mechanical shutter requires the X-ray source to be fired for longer periods of time. This could create excessive anode heating. The temporal resolution of thermionic sources has been improved with more sophisticated power supplies, faster rotation speeds, and clinical implementation of two X-ray source and detector pairs in a single CT scanner.

2.3 Carbon Nanotube X-ray generation

2.3.1 Motivation

A CNT cold cathode has been invented in order to address the limitations of the thermionic X-ray source. The CNT X-ray source uses electron field emission to generate electrons from the cathode. This design is more compact than a thermal emission cathode allowing multiple X-ray sources to be mounted within a single X-ray tube. Since the electrons are emitted by the creation of an electric field, switching of the X-ray sources can be done with sub-millisecond resolution.

2.3.2 Field Emission

The emission of electrons into a vacuum from the metal cathode is explained in terms of quantum-mechanical tunneling. The total energy of the electron in the cathode is lower than the barrier potential. The metal has an intrinsic potential where the Fermi level is filled with electrons. The vacuum energy is the potential energy of an electron at rest outside of the metal. The energy difference between the Fermi level and the vacuum energy level is known as the work function (ϕ). In a strong electric field, electrons can tunnel through the surface potential barrier into the vacuum. This can be seen in figure 2.3 where the tunneling distance is decreased by a strong electric field. The smaller the tunneling distance, the greater probability of an electron tunneling.

The process of the extraction of the electron from a solid by tunneling through the surface potential barrier is governed by the Fowler-Nordheim theory.(**?**) The Fowler-Nordheim equation describes the current density, *J*, of the tunneling.

$$J = \frac{aF^2}{\phi} exp\left(-\frac{b\phi^{3/2}}{F}\right) \tag{2.1}$$

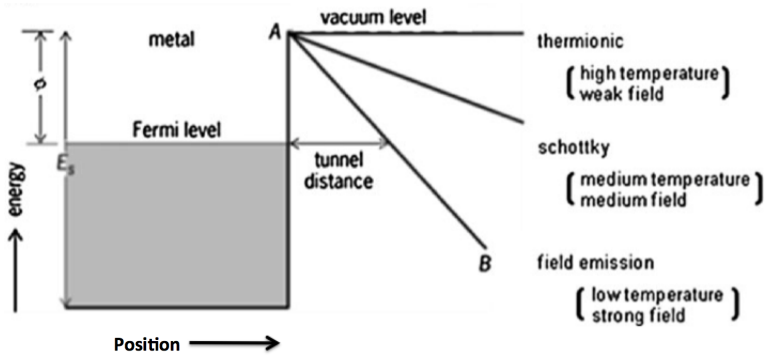

Figure 2.3: A schematic showing the Fermi energy within the metal cathode is lower than the vacuum potential. The difference in energy is known as the work function, (ϕ). By applying a strong electric field, the tunneling distance is reduced and electrons can escape the cathode. (Hamanaka et al., 2013)

Where a is a constant equal to $1.54 \times 10^{-6} A \cdot eV \cdot V^{-2}$ and b is a constant equal to $6.83 eV^{-3/2} \cdot V \cdot nm^{-1}$, F is the applied electric field.

This model shows the dependence of the emitted current on the electric field and the work function. The electric field is dependent on the shape of the metal, voltage applied, and the distance between cathode and anode. (Hamanaka et al., 2013) Since the current of electrons is dependent on the applied electric field, the temporal resolution of the CNT cathode is significantly better than a thermal emission cathode.

2.3.3 CNT Field Emission

CNTs are good field emitters due to their high aspect ratio, strength, high electrical and thermal conductivity, and resistance to oxidization. The high aspect ratios enhance the electric field. The electrical conductivity makes it easier for the electrons to tunnel out of the metal. The thermal conductivity reduces the heating of the cathode. Their strength and resistance to oxidization keeps them from burning during the high currents.

2.4 Components of a CNT X-ray source

A CNT X-ray source is made of four main parts: CNT cathode, gate electrode, focusing electrodes, and anode. In order to make the cathode, CNTs are deposited onto a highly conducting substrate such as molybdenum. A scanning electron microscope (SEM) image of the deposited CNTs is shown in the insert of figure 2.4. The exact cathode specifications are determined by the use of the

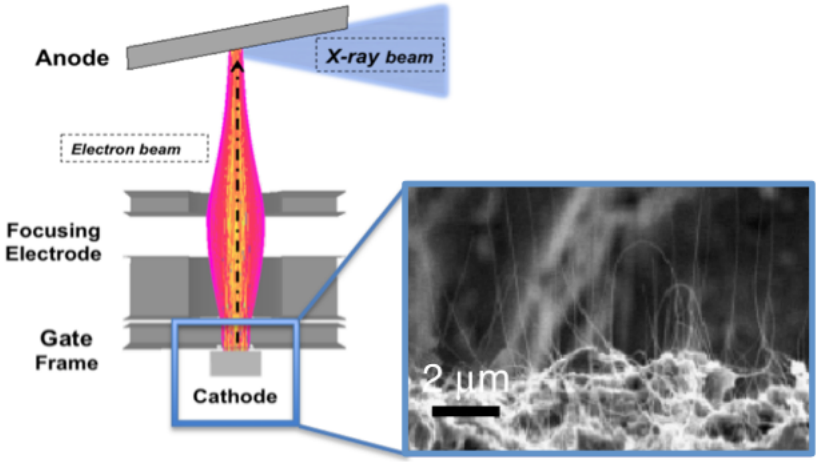

Figure 2.4: The left side shows a schematic for a CNT X-ray source. The molybdenum substrate is coated in CNTs. A positive bias is applied to the gate allowing for electron field emission from the CNTs. The electrons are then focused and collide with the anode. X-rays are produced at a 90° angle to the incident electrons.(Zhou and Calderon-Colon, 2010)

X-ray source. The size of the cathode will effect the focal spot size and maximum current from the cathode.

The electrons are pulled from the cathode when the gate electrode is given a positive bias, creating an electric field between the cathode and gate mesh. There are two designs that will produce a positive bias. The first is a grounded cathode and a positive voltage around 1-2 kV. The second design is a grounded gate and a negatively biased cathode. The gate mesh is commonly made of tungsten.

The emitted electrons have a wide angular span. In order to focus the electrons to the desired spot on the anode, focusing electrodes are used. These electrodes provide an additional electric field to decrease the size of the focal spot on the anode. The anode voltage in the CNT X-ray sources can vary from 24kV for mammography imaging to 140kV for CT imaging.

This cold cathode design is more compact than a conventional cathode. The components of the X-ray source are shown in figure 2.4. These CNT cathodes could be put into any configuration to create a multi-pixel X-ray source array. The most common configuration for medical applications is a linear array.

2.4.1 Limitations of CNT X-ray source

There are limitations to the CNT X-ray source design. One of the limitations that arise from the CNT X-ray source design is the relatively small X-ray flux, compared to a conventional X-ray source. A larger amount of electrons generated from the cathode, known as tube current, allows for shorter X-ray pulses which decrease the imaging time. The X-ray source current is limited by the thermal management of the anode. If a rotating anode were to be used, a larger X-ray flux could be used. The current CNT X-ray sources in use have a tube current between 1 and 80mA.

The amount of voltage applied to the gate cathode needed to yield a fixed current can change over time due to the changes in the CNT X-ray sources. The CNTs can burn out, reducing the amount of current passed through or they can elongate, increasing the amount of current that is produced. In order to address this, the amount of current from each X-ray source is measured every time it is fired, that data is fed back into the voltage supply of the gate. Then, automatically, the voltage applied to each gate is fine-tuned to maintain constant output.

Another limitation of the multi pixel X-ray sources the risk of current arcing between the sources at a high anode voltage. Arching can occur if there are contaminants in the X-ray tube. The contaminants can ionize from the heated tube components or environmental contaminants; these ions can cause arcing. In order to prevent arching, the X-ray source is in a vacuum, typically 10^{-8}torr.

2.5 Applications of CNT X-ray sources

The CNT X-ray source has been used in radiation treatment and X-ray imaging applications. For radiation treatment, a micro beam radiation therapy (MRT) system has been developed and that has shown promising results in mice. (Chtcheprov et al., 2014) A photo of this system is shown in in figure 2.5. The CNT cathodes has allowed for multiple X-ray sources with multiple focal tracks as small as 100 μm wide to be combined in a single system. Previously, MRT could only be accomplished at synchrotron facilities.

The CNT X-ray source has also been integrated into a stationary digital breast tomosynthesis system (s-DBT). (Qian et al., 2012; Tucker et al., 2014; Calliste et al., 2015) A schematic can be seen in figure 2.6(a). The first generation s-DBT system is undergoing clinical trials, shown in figure 2.6(b). The second generation system has been fabricated and is currently undergoing

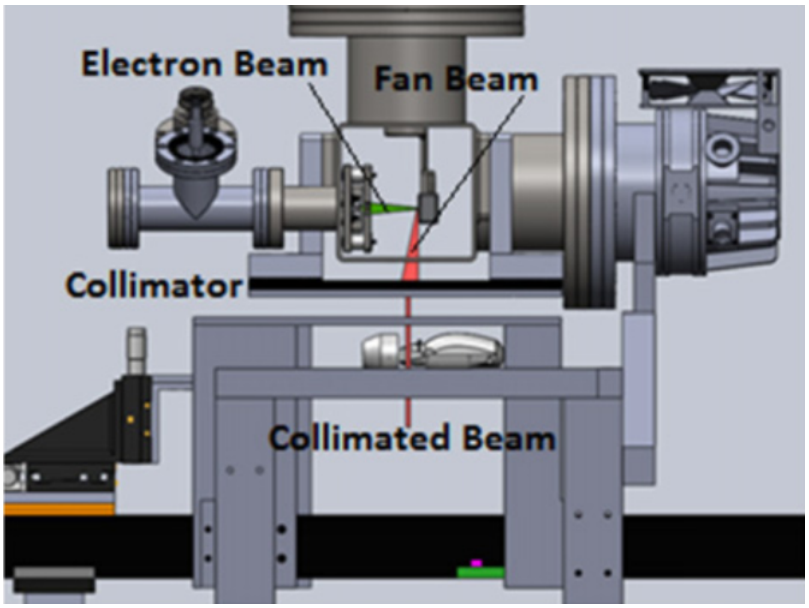

Figure 2.5: A photo of the MRT experimental setup for small animal imaging.(Zhang et al., 2014)

conditioning and characterization. Digital breast tomosynthesis (DBT) is now FDA approved for screening of breast cancer. The CNT X-ray source has allowed for a full DBT motion to be acquired with no mechanical motion. This decreases the focal spot motion blur that degrades DBT's ability to distinguish malignant from non-malignant micro-calcifications.

An intra oral digital tomosynthesis system was created and tested to aid in diagnosis and treatment planning of dental disease.(Shan et al., 2015b) The stationary intra-oral tomosynthesis unit was shown to have image quality equivalent or superior to standard digital images with the added benefit of 3D information. This system is currently installed in the UNC dental school for ongoing clinical trials. Due to the compact nature of the CNT multi-pixel X-ray source, 3D intra-oral imaging is being tested as a screening tool for tooth fractures and cavities.

The micro-computed tomography (micro-CT) system was used to gain respiratory and cardiac gated images in small animals with high spatial resolution. There have been two micro-CT systems built that will be discussed in later chapters.(Burk et al., 2012; Cao et al., 2010). A CAD drawing of the first MRT system can be see in figure 2.7. The CNT X-ray source with fast temporal resolution allowed for cardiac and respiratory gated imaging in mice studies.

A stationary digital chest tomosynthesis (s-DCT) system is another application of the CNT X-ray source. This system is discussed in detail in future chapters.

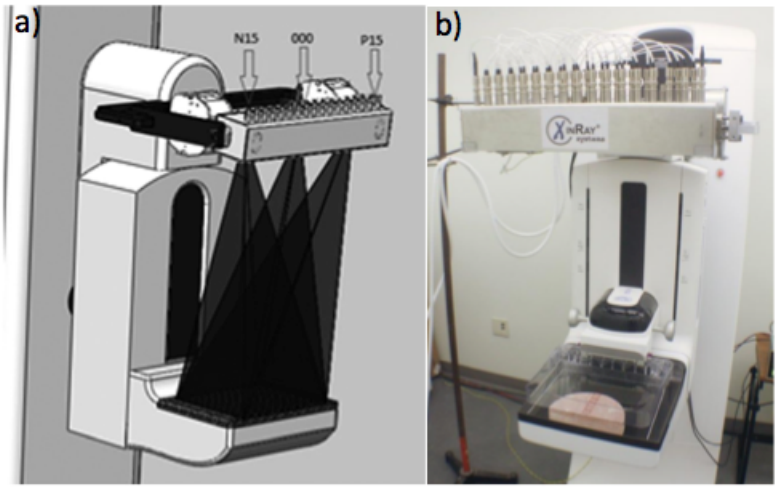

Figure 2.6: (a) A schematic for the s-DBT system showing the multiple CNT X-ray sources illuminating the whole detector (b) A photo of the s-DBT system installed in the UNC hospitals for clinical trial.(Tucker et al., 2013)

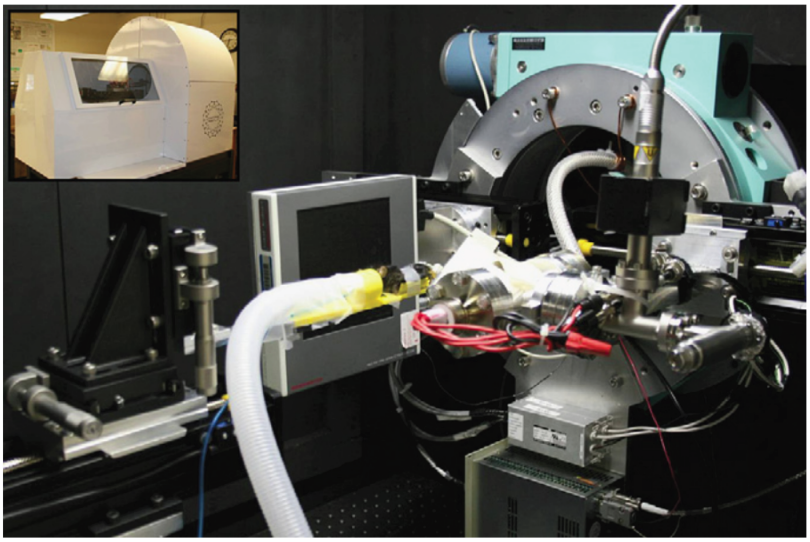

Figure 2.7: A photo of the Micro CX-rayT system setup for small animal imaging. (Cao et al., 2010)

2.6 X-ray Image formation and quality assessment

2.6.1 X-ray Attenuation

X-ray images are acquired using shadows of the X-ray beam passing through the subject. The X-rays could pass through the patient with no attenuation or be attenuated by either absorption or scattering. These attenuation events affect which and how many X-ray reach the imaging detector. When an X-ray is absorbed by tissue in the body, the energy from the photon is dispersed in the tissue. This can cause ionizing radiation that can have negative biological effects. When a photon is scattered, the direction of the photon could be changed. Detecting a scattered photon is the cause of noise in the image and degrades image quality.

For a monochromatic X-ray source, the intensity of the X-rays passing through a medium is described by this equation:

$$I = I_0 e^{-\sum_i \mu_i x_i} \tag{2.2}$$

where I is the output intensity, I_0 is the input X-ray intensity, μ is the mass attenuation coefficient for the material, and x_i is the distance traveled in that material. This equation shows that the X-ray absorption in the materials along the path between the X-ray source and X-ray detector are summed together to find the total attenuation of the medium. The difference in attenuation of different anatomical structures gives contrast in an image.

Figure 2.8 shows a graph of the common mass attenuation coefficients where μ is the attenuation coefficient and ρ is the mass density of the material as a function of energy. This graph shows that the attenuation of soft tissue and fat are very similar around the 80 - 120 keV range where lungs are typically imaged. This means that it is harder to differentiate the fat from soft tissue. However, bone has a higher attenuation provides good contrast against the background of the chest field of view. The K-edge causes the sudden increase in the attenuation coefficient of the material. This occurs at the energy above the binding energy of the K-shell electron, in this case of lead and iodine respectively. A photon having an energy just above the binding energy is more likely to be absorbed than a photon just below that energy.

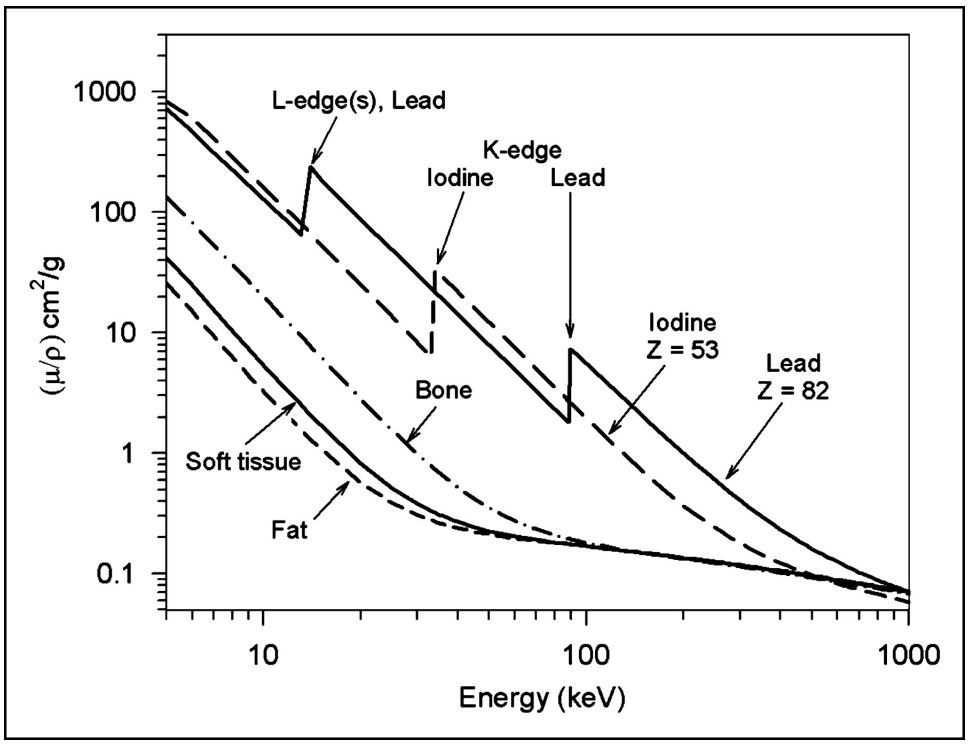

Figure 2.8: This graph shows the mass attenuation dependence on the energy of the photons passing through it. Mass attenuation coefficient is the attenuation coefficient of a material, μ dividend by the mass density of that material ρ as function of X-ray energy. The contrast of an X-ray image comes from the difference in attenuation between anatomical features. This graph shows that fat and soft tissue have similar attenuations around 80 keV, therefore, it would be harder to distinguish between those two structures in an X-ray image. (Seibert, J. Anthony, Boone, 2005)

2.6.2 X-ray Detectors

The X-ray detector measures the spatial distribution and intensity of the photons as they hit detector. Medical imaging detectors are flat panel detectors that could be indirect or direct.

An indirect detector uses a scintillator material to convert an X-ray to visible light, then the visible light is detected. Each pixel contains a photo diode that generates a small current proportional to the intensity of light produced by the scintillator layer on the front of the pixel. After the image is acquired, the gray value of each pixel is read out to a command processor.

A direct flat panel detector uses a high voltage bias electrode and amorphous selenium. Electrons are produced by the interaction of X-ray in the selenium and are collected in the storage capacitor of each pixel, then the capacitors are discharged and the current of each pixel is read out to a command processor.

The command processor converts the current read out by the pixel into a gray value. This yields a 2D array of gray values that form an image.

2.6.3 Image Quality Parameters

The purpose of medical imaging is to help medical professionals understand and diagnose internal structures and functions of their patients. The ability of the medical professionals to gain diagnostic information from the images depends on the quality of the image. There are two main components to diagnostic image quality: contrast and resolution. These image quality parameters effect the sensitivity and specificity to the images.

Contrast quantifies the difference between characteristics of an object and surrounding background. (Prince and Links, 2006) High contrast allows for easier identification of individual objects in an image. An effective way to quantify contrast is to examine the modulation of a periodic signal. The modulation quantifies the relative amount the signal stands out from the average background in an ROI.

The contrast can be degraded by noise in the system. The signal to noise ratio, (SNR) is the ratio of primary signal to noise in an image. The primary signal is the X-rays that leave the X-ray source and arrive at the detector with no scatter. The noise of the image is scattered X-rays that are detector by the detector. A higher signal to noise ratio will result in better contrast. It is commonly calculated

by dividing the average signal value of a region to the standard deviation of the gray values in the same region. The SNR can be an indicator of sensitivity of the system.

Resolution is the ability of an imaging system to depict details. Image resolution quantifies how close two lines can be to each other and still be visibly resolved into separate structures. In order to calculate the resolution of the system, a thin tungsten wire is imaged. A line profile is then made orthogonal to the imaged tungsten wire. The line profile becomes the line spread function (LSF). The resolution of the system can be represented by the full width at half maximum (FWHM) of the LSF. The FWHM of the LSF is the minimum distance two lines must be separated in order to appear as separated in the recorded image. (Prince and Links, 2006) The 1D Fourier transform of the LSF yields the MTF of the system. Therefore the MTF can effectively compare medical imaging systems in terms of contrast and resolution. The calculation of the MTF will be discussed in Chapter 3).

2.7 Key factors in gating

2.7.1 Introduction to gating

Imaging of the chest has many complicating factors. First, there are many overlaying chest structures such as the ribs, heart, and lungs that can mask disease and impede proper diagnosis. Secondly, breath holds can be difficult for sick patients. This can induce motion blur and reconstruction artifacts into the images.

It has been shown that the main factor in image degradation during 3D imaging is patient motion blur, even in images taken during a single breath hold.(Johnsson et al., 2014b) This is largely due to the long scan times inducing global patient motion blur and physiological motion blur. Currently, patients not capable of a breath hold are either given a CXR instead of a CT scan, or are sedated and intubated. Patients not capable of a complete breath hold are excluded from DCT trials.

In order to address the challenges of chest imaging, gated imaging has been developed. This section will cover some key factors in gating such as types of gating, image degradation,and temporal coincidence.

Types of gating Gated imaging is the process of acquiring images during normal physiological processes that are then reconstructed to obtain diagnostic information. There are mechanisms of gating: predictive, retrospective, and prospective. Predictive gating calculates when the desired physiological

process will occur and acquires images at that time in the future. Predictive imaging is very reliable for cardiac imaging. Retrospective imaging acquires images throughout the physiological cycles and sorts the images based off of the phase they were acquired in. In X-ray imaging, the radiation dose associated with retrospective imaging is very high. Prospective imaging is acquiring images in real time during the physiological process is occurring. (Lell et al., 2009)

Image degradation In 3D imaging, there is some inherent image degradation due to the multiple projections needed to reconstruct a 3D image. There are three main types of motion blur in images: X-ray source, global patient, and physiological motion blurring.

There is X-ray source motion blur, this is blur due to the motion of the X-ray source while it translates. This is mitigated by a step and shoot technique while imaging, but can elongate the scan time. An image would have streak artifacts in the scanning direction in the projection images if X-ray source motion blur were present. In modern CT and DCT, X-ray source motion blur is not a major factor to image degradation due to the high flux X-ray sources. When the X-ray source has a high flux, the exposure time is low, therefore the translation time of the X-ray source during an exposure is small.

Long scan times can increase global patient motion blur. This type of blurring comes from patient's inability to stay still for prolonged periods of time. This blurring is apparent when looking at the posterior ribs of a patient. If the posterior ribs of the patient are blurred, then it is likely due to global patient motion blur.

Physiological motion blur, mainly cardiac and respiratory motion blur, also degrade image quality even when the scan is taken within a single breath hold. Cardiac blur can be seen by artifacts, shadowing, or blurring at the heart edges in the reconstructed images. Respiratory motion blur is easily spotted by looking at the edge of the diaphragm. The diaphragm will have artifacts, shadowing, or blurring if the patient struggled to hold their breath during the scan.

Gated imaging is a way to limit cardiac and respiratory motion blur. Gated chest imaging was first implemented for cardiac imaging in CT systems. Gating is required for most 3D cardiac imaging due to the fast cardiac cycle. CT scanners are able to gate to the cardiac breath hold both retrospectively and predictively.

Temporal coincidence Most gating is driven by the temporal coincidence of the system. When the inspiration phase of the respiratory signal is being isolated, in order to acquire an image, the patient must be at peak inspiration, the detector must be counting photons, and the source must be in the desired position to acquire the image, this is called temporal coincidence. In order to increase temporal coincidence, the X-ray detector may be slowed down to increase the integration time or the window of the physiological cycle to be captured could be increased.

2.7.2 Applications of gating

Predictive gating on a CT scanner Predictive imaging allows for cardiac imaging without significantly increasing the radiation dose of the CT scan. In predictive gating, the diastole phase of the heart cycle is isolated because it is the most still phase of the heart cycle. The time when the diastolic phase of the cardiac cycle will occur is estimated from the prior 3 to 7 heart beats. During the scan, the motion of the X-ray source, heart, and the patient table translation must all be synchronized. As a result some heart beats are skipped during imaging, causing an increase in the scan time. For a single slice CT, it takes roughly 48 heartbeats to take an image, for a DSCT it takes roughly 24 heart beats. The z-axis resolution is limited so the entire heart area can be imaged in a single breath hold. This method is only effective for heart beats less than 90 beats per minute, any higher rate and the diastole phase is not long enough to predictively gate.(Rasmussen et al., 2015; Nicolaou et al., 2008) When predictive gating is not possible, retrospective gating may be possible. In retrospective gated scanning, images are acquired continuously and the ECG signal is recorded. The images are then sorted based on the phase of the heart they were acquired. For images to be reconstructed, every position of the heart must be covered by a detector row at every point during the cardiac cycle. Retrospective gating requires a large radiation dose due to the large number of projections needed. (Desjardins and Kazerooni, 2004)

A single source CT scanner, using a high pitch mode, has a temporal resolution of between 250ms and 350ms. (Petersilka et al., 2008) The temporal resolution for a CT scan is the number of views per segment multiplied by the time of repetition. Therefore to increase temporal resolution, the rotation speed is increased. In order to increase the temporal resolution, DSCT scanners have been applied. Using a dual source system, the temporal resolution is greatly improved to 75ms.(Petersilka et al., 2008)

For patients with a heart beat above 90bpm, the temporal resolution of a conventional CT scanner is not high enough to image the heart predictively. In this case, retrospective gating can be used. In retrospective gating, images are acquired continuously through the cardiac cycle. The images are sorted and reconstructed. These images can give some functional information about the cardiac cycle. A large radiation dose is needed for these scans.

Prospective gating with a CNT X-ray source The fast switching of the CNT cathodes allows for real time prospective gated imaging. This has been shown in a micro-CT mouse studies on two generations of micro-CT scanners.(Cao et al., 2009, 2010) The micro-CT system contained 1 CNT cathode and a high resolution detector. The temporal resolution for these studies was limited by the flux of the X-ray source. Therefore the temporal resolution for the first generation tube was 50ms and for second generation tube, 15ms. These studies showed the feasibility of high temporal resolution switching in a CNT X-ray source.

The bench-top prototype for the s-DCT system completed a proof of concept study using the CNT X-ray source array and a dynamic chest phantom. This study showed that a multipixel X-ray source could reduce motion blur in gated imaging by 85.7% (Shan et al., 2015a).

CHAPTER 3
Research Aim 1: Create clinical prototype of s-DCT

3.1 Introduction

As discussed in the previous chapter, the multi-pixel CNT x-ray sources have shown promising results in many applications. The focus of this dissertation is on the s-DCT system. This chapter will provide the motivations, background characterization of the system, materials and methods, important system parameters, and preliminary studies done on the non-gated clinical configuration s-DCT system. This s-DCT system started as a bench top proof of concept study and was transitioned to the Biomedical Imaging Research Center (BRIC) in Marsico Hall for clinical trials.

3.2 Motivation

Computed tomography (CT) is the current gold standard for lung imaging. CT provides a 3D representation of the chest anatomy and produces a stack of images at different focal planes within the patient. This limits the loss of sensitivity due to tissue overlap. A CT scanner uses a conventional x-ray source and detector fixed on a rotating gantry. The rotation allows the CT scanner to acquire $\sim$1000 projection images at different angles with respect to the patient in a helical path. Recently dual source CT scans have been developed. The dual source systems cut the scan time in half due to the dual x-ray source and detector systems.

The projection images are then reconstructed into a high contrast stack of images with each image showing a different plane within the patient. A limitation of a CT is that it requires an effective radiation dose of between .5 and 3 mSv. (Mott et al., 2013) Due to the high dose, CT is not ideal for repeated screening for lung disease or routine follow ups. Another limitation of a CT scan is the relatively long scan time ($\sim$5-10s) (Von Steyern et al., 2012) . During that time, patients are instructed to hold their breath. If the patient breaths during the scan, the image quality can be significantly degraded.

In order to address the limitation of the large x-ray dose required by a CT, digital chest tomosynthesis (DCT) was created. A DCT scan acquires a small number of projection images over a limited angular range. (Dobbins and Mcadams, 2009; Iii and Godfrey, 2003; Johnsson et al., 2014a) For a DCT scan, a conventional x-ray source is on a translating gantry but the detector is stationary under the patient. A DCT scan requires a dose of about 1/10th of a CT scan because a smaller number of projections are acquired over a smaller angular span. (Vult von Steyern et al., 2012; Sabol, 2009; Vikgren et al., 2008) DCT does not have the sensitivity and specificity of a CT scan but for screening and cystic fibrosis (CF) disease monitoring it has been shown to be a good low dose alternative. (Langer et al., 2016; Meltzer et al., 2016)

There are commercial DCT systems available and their imaging parameters are shown in table 3.1. These DCT systems use conventional x-ray sources therefore the anode voltage, focal spot, and resolution are similar to a conventional CXR system. The DCT systems take between 60-74 images for a chest scan covering an angle of 30°-40°. An increased angular span, will increase the depth resolution in the images. The scan time is 5s-10s. This scan time is limited by the need to mechanically move the x-ray source. Overall, the system resolution, measured as MTF, is roughly 3-3.5 cycles/mm for the commercial DCT systems. The resolution is limited by the focal spot size, the detector pixel size, and the imaging dose. The effective dose of the DCT scans are between .12mSv and 1.2mSv. Increasing the resolution of the system would increase the dose required to image the patient.

The greatest limitation of the a conventional DCT system is the long scan time. In clinical trials, pediatric patients are excluded due to their inability to complete a breath hold. In order to address the limitations of the DCT system, the s-DCT system was created. Due to the stationary CNT x-ray source array, the entire DCT scan can be acquired without mechanical motion. This allows for faster scan times and the ability to do prospectively gated imaging.

3.3 Materials and methods for non-gated s-DCT system

3.3.1 System overview

The s-DCT system is comprised of a CNT x-ray source, flat panel detector, computer, switching system, and electronic equipment to power the system. The images are taken along the z-axis, parallel

	Conventional DCT Systems		
Commercial System	**GE VolumeRAD**	**Shimadzu Safire**	**s-DCT system**
Anode (kVp)	80-120	80-120	80
No. Projections	60	74	31
Ang. Coverage (°)	30 -35	40	12
Scanning Time (sec)	10	5	10
Focal Spot Size (mm)	0.6/1.2	0.4	2.5 x 0.5
Effective Dose (mSv)	.12	***	***
Resolution (cycles/mm)	3.5	3	1.7 x 3.4

Table 3.1: A comparison between two commercial DCT systems and the s-DCT system. (Dobbins et al., 2008a; Vikgren et al., 2008; Båth et al., 2010; Li et al., 2008; Yamada et al., 2011)

to the patient's spine. Figure 3.1 shows the clinical configuration of the s-DCT system installed in the BRIC on the UNC campus. The electronics rack holds the equipment that will be discussed in later sections. The flat panel detector is embedded in the mattress, under the sheet. The x-ray source is shown mounted above the patient bed. The x-ray source has been covered with white acrylic. Also under the cover, x-ray filtration and collimation ensure the x-ray field meets all radiation safety regulations. Behind a leaded wall (not shown in this picture) is a tech work station with a computer to control imaging. This system has been electrical safety and radiation safety certified. System topology can be found in 3.2.

3.3.2 s-DCT x-ray source

This XinRay x-ray source (Model 2008-08-L75-002, XinRay System Inc., Research Triangle Park, NC) was designed for alternative experiments and was retrofitted for medical imaging purposes. Some of the specifications of the x-ray source are not optimal for medical imaging. A schematic drawing of the CNT x-ray tube is shown in figure 3.3a. The schematic shows how each individual CNT x-ray source covers the same area of the detector using a cone beam. This allows the system to acquire images at multiple angles with respect to the detector without any mechanical motion.

The x-ray tube used in this experiment is shown in 3.3b. This x-ray source has 75 independent focal spots distributed in a 29cm linear array. For this study, 29 of the focal spots were used with an 8mm pitch. Due to the 29cm length of the tube, using all 75 focal spots would over sample the image space. This would increase the patient dose without increasing the image quality. The focal spot size was measured for each of the sources and the average was 2.5mm x .05mm. (Shan et al.,

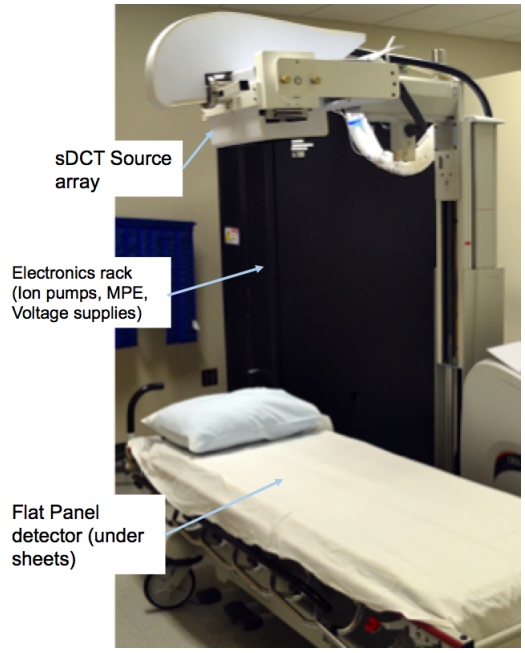

Figure 3.1: A photo of the clinical configuration of the s-DCT system. The CNT x-ray source array is covered and mounted above the bed. The electronics rack holds the equipment to monitor and drive the system. The flat panel detector is embedded in the patient bed mattress.

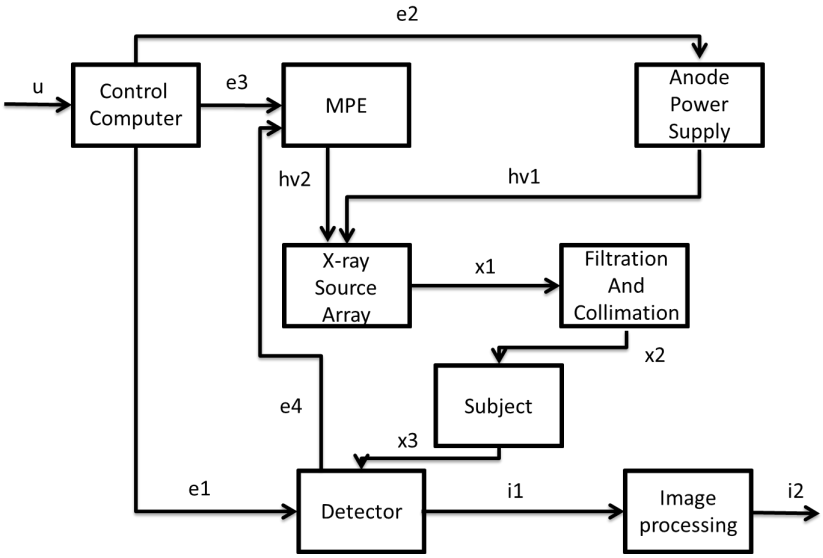

Figure 3.2: The topology of the s-DCT system. u- User setup of control computer, e1- initiation of the detector, e2-initiation of anode power supply, hv1- apply high voltage on the x-ray source array, e3- initiation of MPE after hv1 reach the targeted voltage, e4 - Trigger to MPE for x-ray pulses, e5- After signal e4, the pulse train is sent to the Control Computer and Cathode Switching System. Each pulse represents a single detector acquisition, hv2 - Each signal in the pulse train will activate the Cathode Switching System and apply a voltage to the corresponding cathode which produces a current, x1 - x-rays are produced during each pulse of the cathodes., x2 - x-rays are filtered, x3 - X-rays interact with the object that is in the field of view of the detector, i1 - A raw image is produced for each pulse, i2 - Raw images are processed and reconstructed on a secondary computer.

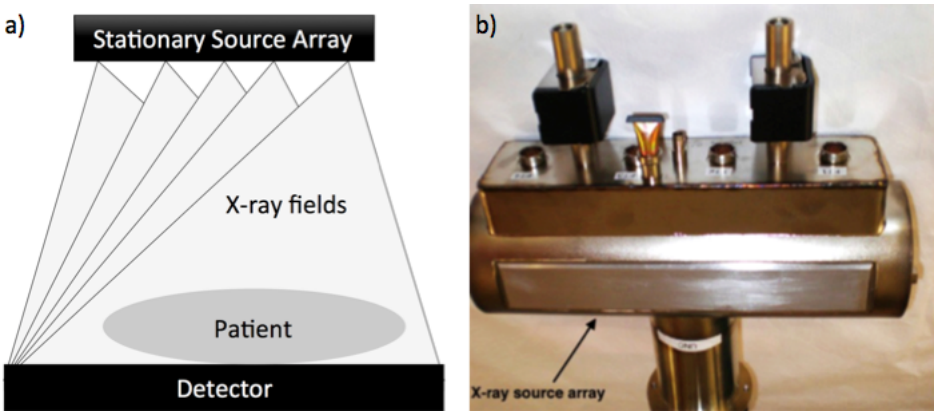

Figure 3.3: (a) The schematic for the s-DCT x-ray source array. Each pixel of the x-ray source illuminates the entire detector field, allowing for a complete tomosynthesis scan with no mechanical motion. (b) The x-ray tube used in this experiment. It is 29cm long with 75 cathodes. The collimation is placed parallel to the x-ray window shown here.

2014a) The focal spot was measured using the pin-hole method described by European standard EN12543-2.(Shan et al., 2013)

For the clinical configuration, each of the 29 individual cathodes output 5mA current. A high voltage switching system controlled the voltage across the gate. The voltage across the gate controls the electric field acting on the CNT cathode. The electric field determines the current drawn form the cathode. The gate voltage was produced by a XinRay switching system (Research Triangle Park, NC, Model 10524602), also known as an multi pixel electronics (MPE), that had a port for each cathode. Therefore, the current from each cathode is independently electronically controlled.

The electrons pulled from the cathode then bombard the anode. The anode in this system is set to 80kVp for imaging. A Spellman high voltage power supply (Hauppauge, NY, model XRV160P1800) powered the anode. The tungsten anode was elongated and shared by the cathodes. In order to comply with the US Food and Drug Administration (FDA) regulations(Adm, 2013) on beam quality for diagnostic imaging, the X-rays were filtered using 2.8mm of aluminum filtration. The x-ray beams are then collimated in the scanning direction. Tungsten bars are fixed 2cm below the scanning window and run the length of the x-ray window. This collimation limits the width of the x-ray field to the width of the detector. There was no collimation perpendicular to the scanning direction. To compensate for that, patients are protected with a lead blanket and lead shield during imaging.

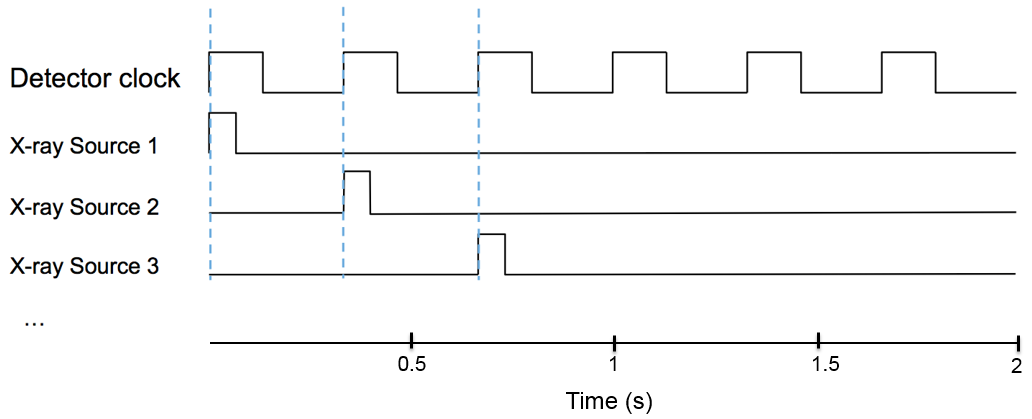

Figure 3.4: A Schematic timing diagram of the triggering system. When the detector clock is high, the detector is integrating, when the detector clock is low, the detector is reading out the image. The x-ray sources are triggered at the rising edge of the detector clock.

3.3.3 Detector

The flat panel x-ray detector was a Carestream Health Inc. (Rochester, NC) 35.3cm x 43cm amorphous silicon detector (model DRX-1C) with a pixel size of 139μm in each direction. A scatter reducing grid was not used. The detector was run in a continuous acquisition mode; meaning the detector was constantly integrating and reading out images. Only during x-ray imaging were the images saved to the computer. Because of the continuous acquisition of the detector, the detector acted as the clock for the system. X-rays could only be fired during the start integration phase of the detector. The detector speed was fixed at 3 frames per second (fps). The integration window was fixed at 110ms and read out time was 270ms. The detector speed limited the imaging time in this experiment. The total time to acquire a tomosynthesis set was 10 seconds.

The maximum allowed pulse width for this study was 100ms. To ensure that the whole pulse width was collected during the integration window, the X-rays were always fired at the leading edge of the integration window. The detector signal was read in through a detector box supplied by Carestream. The detector box had an TTL output that indicated the phase that the detector was in. When the signal was high, the detector was integrating and when it was low, it was reading out, as shown in figure 3.4. The detector box had an ethernet output used to transmit images to the computer after imaging.

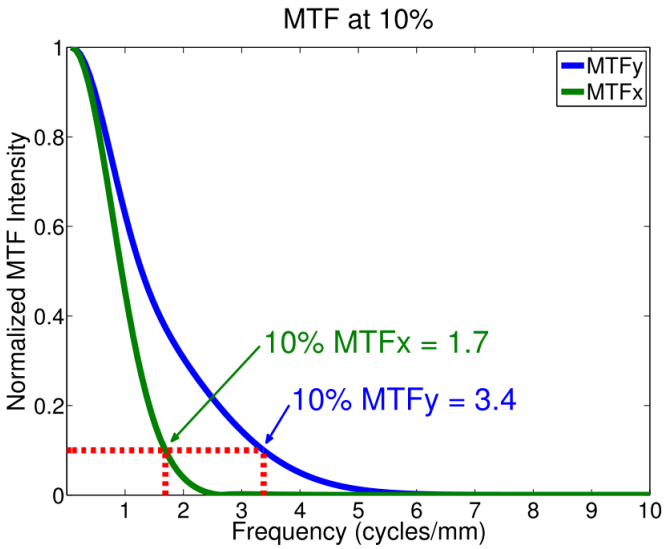

Figure 3.5: The MTF plot of the s-DCT system.(Shan et al., 2013)

3.3.4 System resolution

The modulation transfer function (MTF) is a measure of the in-plane resolution of the system and the artifact spread function (ASF) is a measure of out of plane resolution. Both of these measurements were done with the tube voltage at 80kVp with an SID of 130cm and an SOD of 119cm. Yielding an angular span of 12° covered during imaging.

The MTF of this system was measured to be 1.7 lines/mm in the scanning direction and 3.4 cycles/mm perpendicular to the scanning direction. This is shown in 3.5. The MTF was measured using a 100μm tungsten cross wire phantom. The line spread function (LSF) was measured using the slant angle oversampling method and fitted to a Gaussian function to remove noise. Then the discrete Fourier transform of the LSF was taken to get the MTF. The MTF reported as the was 10% of the MTF function.

The ASF is a good measure of out-of-plane blurring in tomosynthesis images.The ASF is calculated by measuring the contrast between objects and the background in reconstructed images. The ASF was measured to be 5.2 in this system.(Shan et al., 2014a) The ASF is taken by measuring the contrast of the object and it's background. The calculation for the ASF is shown in equation 3.1, where μ is the attenuation of the material. The $\mu_{obj}(z)$ is the gray value of the object when it is in focus and $\mu_{bkg}(z)$ is the gray value of the same region in an image slice above or below the object.

$$ASF(z) = \frac{|\mu_{obj}(z) - \mu_{bkg}(z)|}{\mu_{bkg}(z)} \tag{3.1}$$

3.3.5 System monitoring and control

The s-DCT system was controlled by a LabVIEW program. The flow of this system can be seen in 3.6. The first component of the LabVIEW code monitored the tube health. The anode voltage and tube pressure were measured and displayed for the user to see. The anode voltage was monitored via ethernet cable connected to the computer from the high voltage power supply. The pressure of the x-ray tube was measured via vacuum gauges in the vacuum pumps connected to a Texas International data acquisition board (DAQ). The DAQ read in the analog signal from the vacuum pumps. Monitoring the pressure of the x-ray tube is important to ensure no harm is being done to the cathodes and no arcing between the cathodes. The pressure in the x-ray tube also rises to signify X-rays are firing. The x-ray system automatically shut down if the tube pressure exceeds the safe pressure for the CNTs, typically below $5x10^{-9}torr$. This process is done in the check equipment and initialize modules section shown in figure 3.6

The second component of the LabVIEW code walks the x-ray technician through patient imaging process. This is shown in the event flow in figure 3.6. At the start of an imaging session, a patient was checked into the LabVIEW program. The user inputs the general size of the patient (small, medium, or large) and the identification number.

The size of the patient determined the scout image pulse width. The predetermined pulse width was then programmed into the two channel digital pulse generator (Model DEI PDG-2515) over a general purpose interface board (GPIB) connection. Then, the MPE was initiated to fire the center source one time using an output signal from LabVIEW. After the user starts scout image acquisition, the pulse generator waits for the next trigger from the detector. Upon receiving the detector trigger, pulse generator sends a TRUE signal for the duration of the x-ray pulse width to the MPE. The MPE fires the center x-ray source one time for the duration the pulse generator signal is TRUE.

After the x-ray is fired, the scout image was then read into LabVIEW. The image is displayed and the technician defines the region of interest (ROI) by placing two boxes in the lung region. Then, LabVIEW measured the gray value of the ROI. This region was used to calculate the pulse width

needed to for each cathode to fire to complete a tomosynthesis scan. (This calculation is described in detail in later chapters.)

The tomosynthesis pulse width was then transmitted to the pulse generator. The MPE was initialized to fire all 29 sources in order and then uninitialize. When the user starts the tomosynthesis image sequence, the rising edge of the detector signal triggers each of the 29 sources one at a time, shown in figure 3.4. Then the images were readout from the detector and saved on the computer.

3.3.6 Reconstruction of tomosynthesis images

After the patient is imaged, there were 3 calibration image sets acquired. Images taken with no x-ray field (dark images), with X-rays illuminating the detector with no object in between (air images), and of a geometry phantom (geometry images).

After the patient images were taken the images were pre-processed and then reconstructed into the 3D image stacks. The first preprocessing step was the dead pixel and dark image corrections. The dead pixel correction used a map of the known dead pixels on the detector and averages the value of the surrounding pixels to replace the dead pixel value. The dark image correction used the 24 dark images taken before the x-ray source is turned on. These images were used to correct for electronic noise in the detector.

The next pre-processing step is the off gain correction. The off gain correction uses the air images to correct for inconsistencies in x-ray field. Then the raw images are divided by the air images. This step removes some noise and correct the gain of the images. The preprocessing steps are summarized in 3.2.

$$\text{preprocessed image} = \frac{\text{image - dark image}}{\text{blank image - dark image}} * \text{scaling factor} \tag{3.2}$$

The final preprocessing step was to determine the location of the x-ray source with respect to the detector. This location is crucial for the reconstruction process. The geometry phantom had 4 metal rods connecting 2 sheets of plastic. The location of the top and bottom of each rods was found on each image. From that information, the exact location of each x-ray source with respect to the center of the detector was found. This matrix was output as a geo.mat file. This file was later read into the reconstruction algorithm.

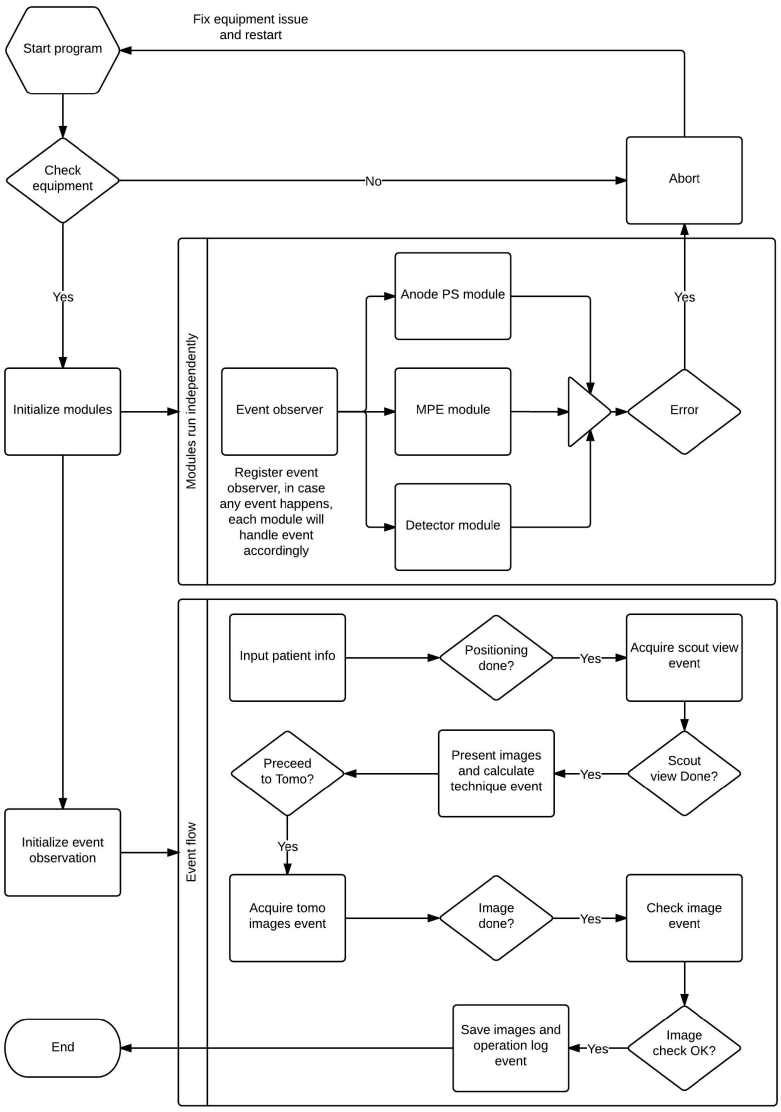

Figure 3.6: A flow chart for patient imaging in the s-DCT system.(Shan, 2015)

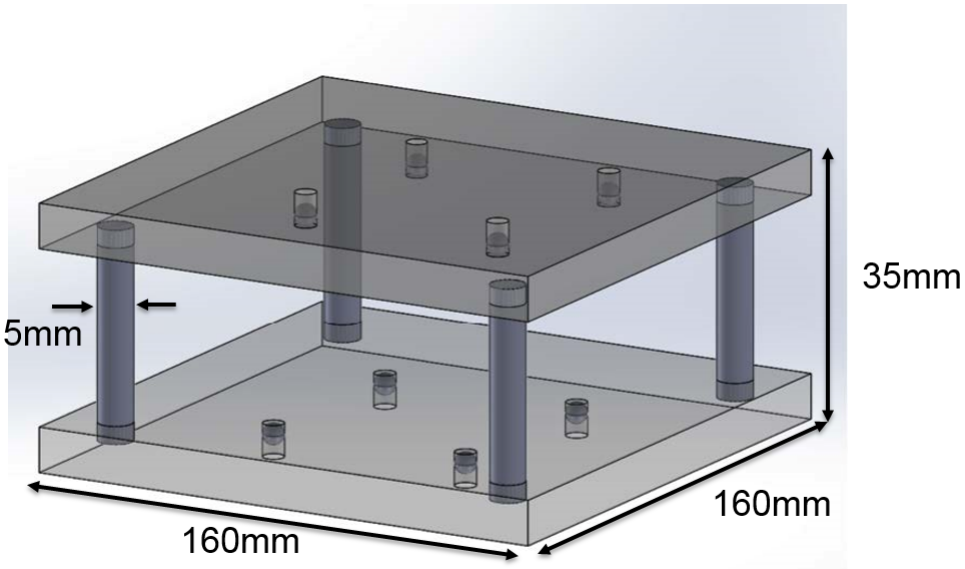

Figure 3.7: CAD drawing of the geometry calibration phantom. Four tungsten bars were placed perpendicular to the acrylic layer. Each acrylic plate had four metal beads embedded inside.(Shan, 2015)

After the images were pre-processed and the geometry of the system was established, the images were reconstructed. The reconstructed algorithm used adapted fan-beam volume reconstruction (AFVR).(Wu et al., 2015) Utilizing the linear source geometry used in the s-DCT system, AFVR breaks the 3D cone beam reconstruction into a series of 2D fan-beam volume reconstructions. In this study, a simultaneous iterative reconstruction technique (SIRT) with 20 iterations for each fan-beam volume reconstruction was used. Image sets were reconstructed with slice thickness of 4mm. The reconstructions were done using a Matlab (Mathworks Inc. Natick MA), the computation time was about 10 minutes on a workstation equipped with a 6-core Intel i7-5930K CPU.

3.3.7 Patient Population

Adult patient populations under three ongoing clinical trials were recruited. The clinical trials focused on CF disease progression and lung nodule detection. Patients in either protocol have been recruited with the assistance of the respective pulmonology clinic or the multi-disciplinary Thoracic Oncology Program at UNC. All studies were performed under the approval of the Institutional Review Board of the UNC. Body mass indexes (BMIs) were limited to $32kg/m^2$ due to the limited flux of the prototype x-ray tube. The CF clinical trial recruited patients with known CF and received

a chest radiograph or non-contrast chest CT within the last 21 days. The lung nodule study recruited patients with known lung nodules who received a non-contrast CT within 14 days.

3.4 Dose delivered to patients

The s-DCT system dosimetry was calibrated by the radiation safety team at UNC. There were two steps to the calibration procedure.

The first calibration procedure was used to calculate the cathode current, milliampere-seconds (mAs), required for a tomosynthesis scan from the scout image. The mAs is directly proportional to the number of photons produced from the x-ray tube. The gray value of the detector is a measure of the number of photons that passed through the patient. Therefore equation 3.3 is a measure of how attenuating the patient is. From that amount, the radiation dose needed to effectively image the patient can be calculated.

Looking at equation 3.3, the value of mAs needed is the quantity that will be calculated. The optimal gray value for the ROI in a scout view was determined from the detector manufacturer to be a pixel value of 17,885. The mAs from the scout image was chosen based off of the size of the patient. The tube current is fixed at 5mA. Using this formula and the known quantities, the optimal mAs for the tomosynthesis scan can be calculated using equation 3.4 .

$$\frac{\text{Dose needed(mAs)}}{\text{Optimal gray value}} = \frac{\text{Dose (mAs) scout image}}{\text{Scout ROI gray value}} \tag{3.3}$$

$$\text{Pulse width} = \frac{\text{Dose (mAs)}}{\text{Tube Current (mA)}} \tag{3.4}$$

The second calibration procedure was to calculate the entrance dose delivered to the patient. In order to do this, the correlation between entrance dose and pulse width was found using a 6cc ion chamber (Accu-pro by RadCal, Monrovia, CA). This correlation is shown in figure 3.8. The adult protocol makes the assumption that the chest height of an adult is 24.5cm. This height was chosen because that is the height of the adult anthropomorphic chest phantom. The pediatric protocol assumes the chest height is 17cm. This is the chest height of a pediatric chest phantom of an 8 year old patient.

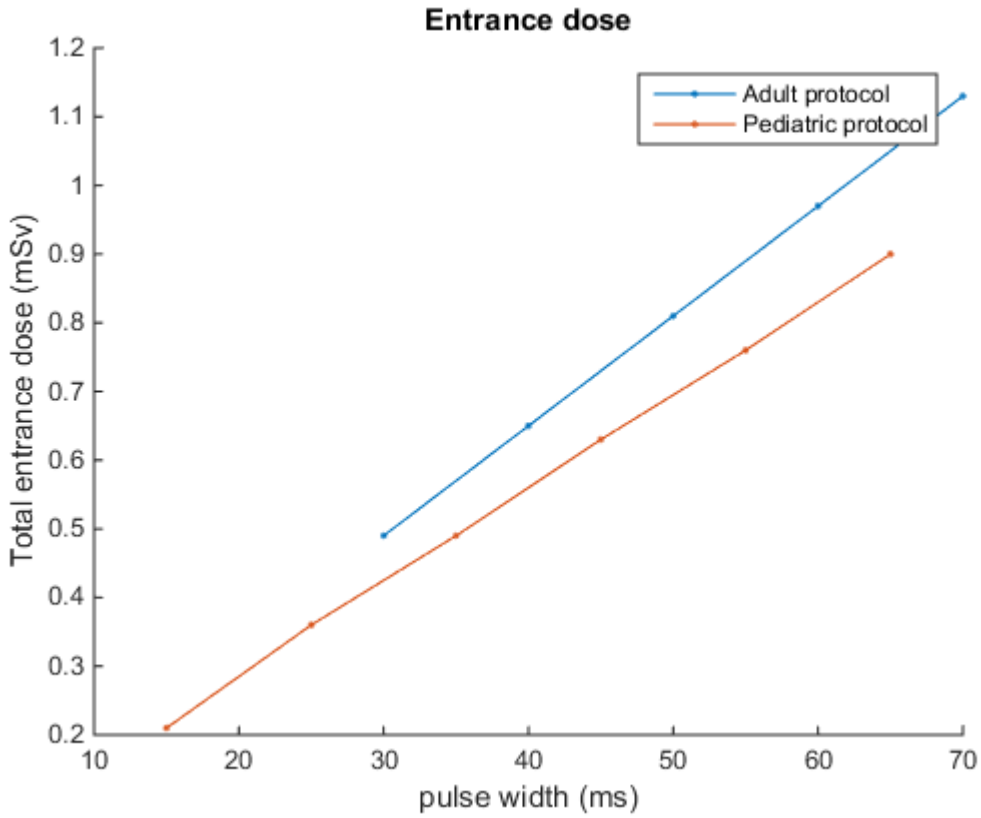

Figure 3.8: The relationship between the pulse width delivered and the entrance dose to the patient. The adult protocol assumes a chest height of 24.5cm. The pediatric protocol assumes a chest height of 17cm.

3.4.1 CXR and CT images

CXR and CT Images were acquired using standard clinical protocols. The CXR images were taken posterior-anterior (PA) prone and the CT images were taken anterior-posterior (AP) supine. The clinical images were collected and anonymized by clinical coordinators.

3.4.2 Image quality evaluation for the CF trial

A preliminary radiologist reader study conducted by three board certified radiologists evaluated a small subset of the reconstructed patient imagines for key lung features. Each reader rated the quality of 6 lung features: lung fields, trachea, proximal bronchi, small airways, diaphragm and lateral costophrenic angles (LCA), and vascular pattern. For each of the lung feature, the image quality was scored between 1 and 5; where 5 was excellent, 3 was fair, and 1 was poor. Thirteen of the 25 image sets collected were evaluated. The model describing this study is taking into account the reader, the field of interest and the subjects (modeled as random factors: we are not interested in the subject effect, however they are taken into account for the variability as results will tend to be similar per subjects).

3.5 Results

3.5.1 Overall patient imaging

As of January 2017, 105 patients have been included in our studies under 3 distinct clinical trials. Of the 105 consented patients, 97 image sets were acquired. Of the 8 failed imaging attempts: 3 were due to the patient accidentally disconnecting the detector tether at some time during the scan, 3 were due to a failure with the MPE, and 2 were due to the patient failing to show up to the scan after filing consent papers.

Of the 97 image sets that were acquired, there were 8 incidents that required manual intervention. Six of the interventions involved manually saving the images after image set was complete. Due to an error with the MPE, the automatic image saving was not initiated. All images were recovered in these cases. The other 2 errors involved manually restarting the detector after the patient was checked in and before the images were acquired. In these cases, all images were acquired normally after restarting the detector.

Since the initial errors in the system were found, the x-ray system has been made more robust by securing the detector tether and better error handling by the detector.

3.5.2 CF Study results

Twenty-one CF patients have been imaged with the s-DCT system. Nine CF patients were in the CT cohort and 12 were in the CXR cohort. The average patient BMI was 22.4±4.3 kg/m^2. The average pulse used was 51.7±15.7ms. This yielded an average entrance dose of 0.62±0.32mSv. Patient ages ranged from 11 to 69 years old.

Reader evaluations by three board certified pediatric and thoracic radiologists show good delineation of thoracic anatomy and depiction of pathological conditions. The overall image quality was rated over 13 patient images in the CF cohort. When looking at the six evaluated regions over three readers and 13 image sets, 77% of the data points were rated as a 4 or 5 depicting good or excellent delimitation, this is shown in Table 3.2. As compared to a CXR image, vasculature, trachea, bronchi, spine, ribs, retrocardiac space, and air trapping are better viewed in tomosynthesis images. Figures 3.9 and 3.10 are images of the first patient reviewed in this paper. Figure 3.9 shows the clinical CXR images taken with an anti-scatter grid in place. Linear markings, an indication of lung scarring, can be seen in the lower right lobe. The ribs are not well defined due to the superposition of the chest structures. This image also shows a poorly defined heart edge. This could be due to the magnification of the heart in a CXR image.

Figure 3.10 shows the reconstructed tomosynthesis slices for the same patient. Figure 3.10(a) is the most anterior slice and Figure 3.10 (c) is the most posterior slice. Figure 3.10(a) is at the depth of the heart. The edge of the heart is represented well, even though the scan was taken over many cardiac cycles. Figure 3.10 (b) shows the same linear marking represented in Figure 3.9 in the lower right lobe. Figure 3.10 (c) shows the spine in focus in the posterior of the patient. This patient did not have any large lesions and no air trapping was found.

For the reconstruction of the lung fields, Reader 3 gave significantly lower rates than the other readers (p-value = 0.0205). The CXR and s-DCT were not found to have significantly different rating in the reproduction of the lung fields (p-value = 0.0744) or trachea (p-value = 0.673). For the reproduction of the proximal bronchi, Reader 2 and 3 gave significantly higher rates for s-DCT than for CXR (Reader p-value = 0.0396, technique p-value = 0.0585). For small airways (p-value

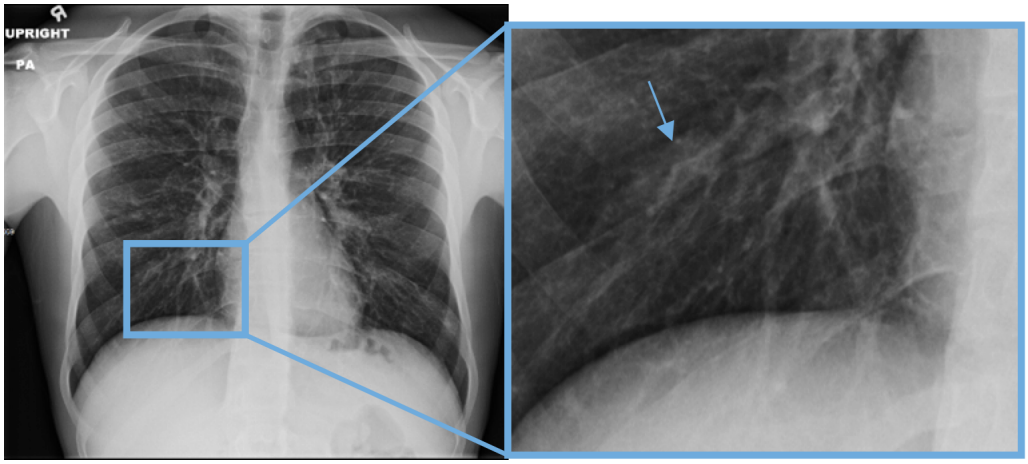

Figure 3.9: A clinical CXR upright PA chest radiograph. The magnified region shows some linear markings

= 0.0241) and vascular pattern (p-value = 0.0193), s-DCT had significantly higher rates than CXR. There was no significant difference in the reproduction of the diaphragm and LCA.

Field	Rate	Frequency	Field	Rate	Frequency
Lung Field	3	11 (23%)	Diaphragm & LCA	3	16 (33%)
	4	22 (46%)		4	8 (17%)
	5	15 (31%)		5	
Proximal Bronchi	2	1 (2%)	Trachea	2	1 (2%)
	3	3 (6%)		3	5 (10%)
	4	15 (31%)		4	20 (42%)
	5	29 (60%)		5	22 (46%)
Small Airways	2	2 (4%)	Vascular Pattern		
	3	18 (38%)		3	10 (21%)
	4	11 (23%)		4	12 (25%)
	5	17 (35%)		5	26 (54%)

Table 3.2: Frequency of each rate per field of interest

3.5.3 LN Study results

There were eighty-four patients with indications of lung nodules included in the study. The average BMI was 25.5±4.2 kg/m^2 and the average pulse width to image the lung nodule patients was 50.7±17.8ms. The average entrance dose was 0.6±0.3mSv.

A lung nodule trial patient image is shown in figure 3.11. The CT was acquired in the conventional supine patient orientation and presented in coronal reconstructions for ease of comparison with tomosynthesis. Tomosynthesis images were acquired in an anterior-posterior (AP) supine view, and

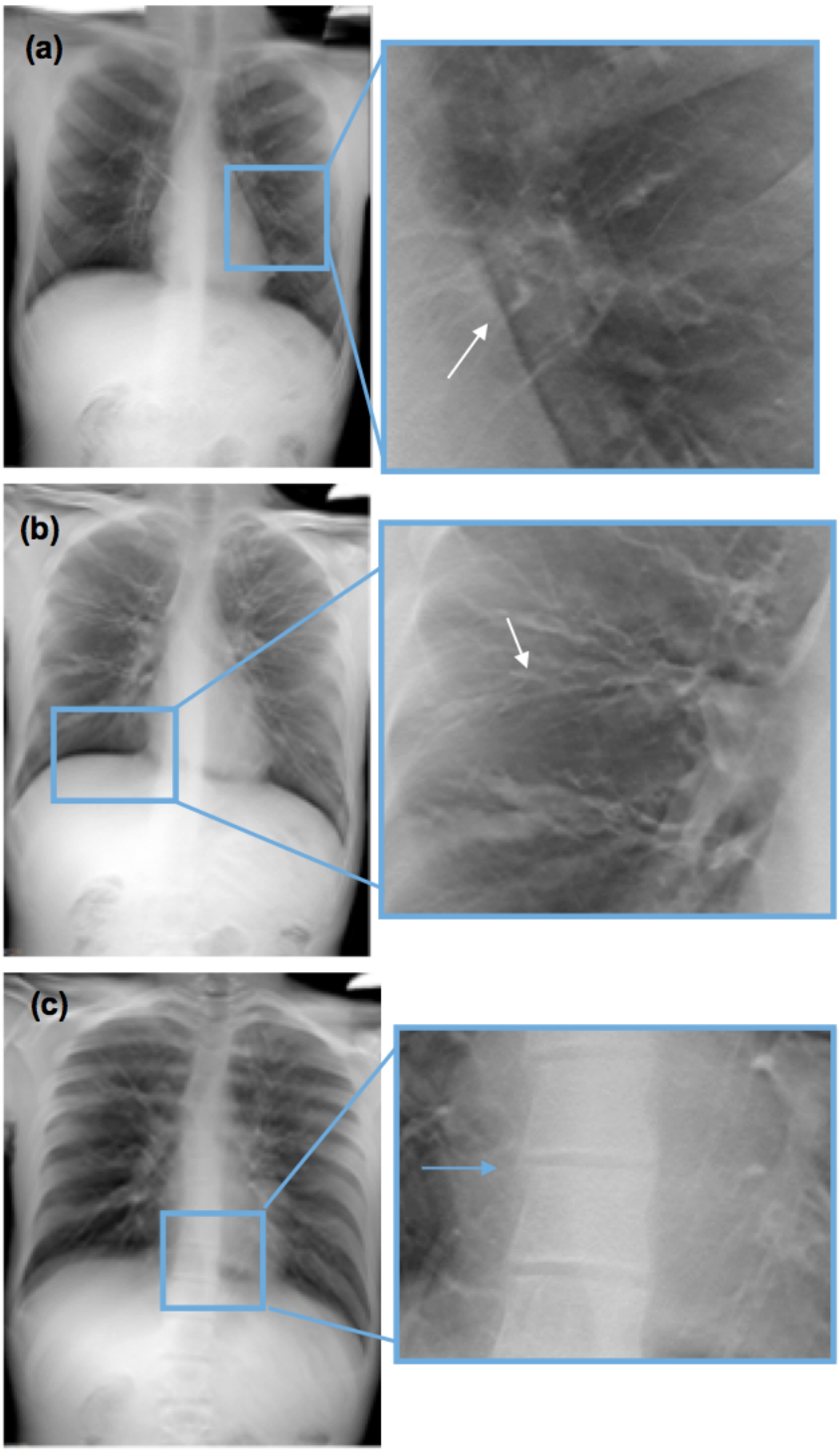

Figure 3.10: Reconstructed image slices from the s-DCT system for patient 2. The most anterior image is (a) while (c) is the most posterior image. Each slice represents a different depth in the patient. (a) The heart is in plane. This is depicted by the sharp heart edge. (b) The vasculature from the middle of the lung is in plane. Linear markings are shown in the insert. (c) The spine and the posterior ribs are in plane.

presented as coronal reconstructions. Figure 3.11(a) shows a slice of a tomosynthesis reconstruction showing a 5.4mm nodule in the lower right lobe. This nodule is also seen in the CT scan, Figure 3.11(b). It was not visible on the recent chest radiograph or CT scout image.

Radiologist readers studies are still ongoing but early evaluations by three board certified pediatric and thoracic radiologists strongly suggest good delineation of the thoracic anatomy and depiction of pathological conditions. Readers reported greater confidence in the s-DCT images as compared to conventional radiographs. Readers reported vasculature structures were almost as well viewed on the tomosynthesis reconstruction as on the CT images. Bone structures, especially anterior ribs and spine, were seen well on the tomosynthesis images.

No significant intraparenchymal respiratory motion blur was seen in any patient image, though cardiac and diaphragm blur was noted by readers on a few patients. Confidence approached that of conventional CT studies in lesions larger than 10mm. Distortions of anatomical structure and larger areas of pathology were identified readily. Smaller lesions (5 mm or less) were more difficult to differentiate.

3.6 Discussion

DCT has been shown to increase visibility of lung pathology over CXR while having a comparable dose.(Johnsson et al., 2014a, 2010) Mucus plugging and airway thickening are well-viewed with DCT.(Von Steyern et al., 2012) Compared to CT, DCT has a lower patient cost (Vult von Steyern et al., 2012; Quaia et al., 2014) and a higher patient turnover(Tingberg, 2010). The sensitivity and specificity of DCT does not yet approach that of CT in identification and characterization of small lung structures.(Langer et al., 2016)

There are some limitations of DCT and s-DCT such as short angular span and long scan time. A short angular span reduces the depth resolution of the system. DCT has an angular span of 30-40°.(Dobbins and Mcadams, 2009; Von Steyern et al., 2012; Terzi et al., 2013a) This limits the view of structures adjacent to pleura, diaphragm, central vessels, and mediastinum.(Meltzer et al., 2016) s-DCT system has a 12° angular span; this small angular span limits the z-axis resolution of the system.(Shan et al., 2014a) This is an inherent limitation of the s-DCT system due to the short length of the x-ray tube. In order to increase visibility of small lung nodules a greater angular span is needed.

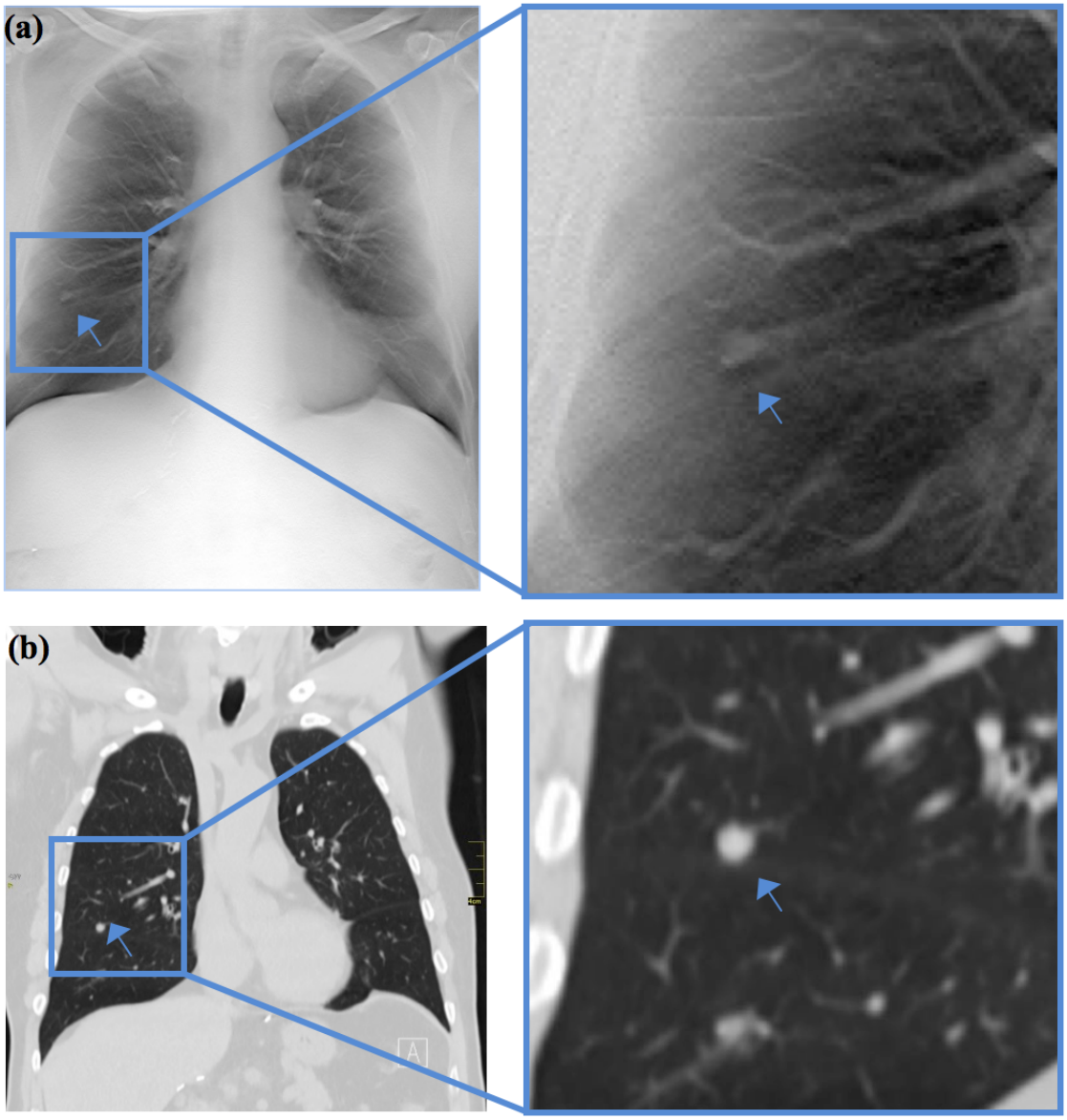

Figure 3.11: Images of a lung nodule study patient. (a) a slice from the tomosynthesis. The arrow is pointing to a small lung nodule about 5.4mm in diameter (b) the same nodule shown in the CT scan.

Another limitation of the current DCT system is the scan time. A typical DCT image set takes about 10 seconds; this is comparable to a CT scan.(Iii and Godfrey, 2003) Young pediatric patients cannot complete a 10 second long breath hold. An incomplete breath hold will cause blurring in lungs and diaphragm decreasing the quality of the image. In order for these patients to get 3D imaging, they must be sedated and intubated for a CT scan. The s-DCT prototype system requires a 10 second scan time. The s-DCT system scan time is limited by the detector speed. With a faster detector in place, the low flux of the x-ray source would limit patient imaging. For the average patient in this study, they could be imaged in 6 seconds using a fast detector. For this study, the low flux of the s-DCT x-ray source did not significantly affect the image quality.

An additional limitation of the s-DCT system is the low anode voltage which limits the penetration of the X-rays during imaging. The s-DCT has been shown to have adequate penetration for patients with a BMI under 32 kg/m^2. There were no signs that the low anode voltage degraded image quality in this study.

The major advantage of the s-DCT system over a conventional DCT system is the array of x-ray sources. Due to the x-ray source array, all projection images are acquired with no mechanical motion. This allows for faster imaging acquisition time without risk of focal spot motion blur. Children are currently excluded from chest tomosynthesis trials due to the need for a breath hold. s-DCT hopes to reduce the need for a breath hold by faster imaging times and implement prospective gated imaging for patients who cannot hold their breath at all.

3.7 Conclusions

Overall, this system has shown promising results in patient trials. The clinical trials are still ongoing and will be evaluated in radiologist reader studies. Thus far, the s-DCT has been shown to have better image quality than CXR. In order to fully utilize the benefit of the multi-pixel x-ray source, prospective gating has been integrated into this x-ray system.

In the course of the present work, the author completed the hardware modifications required electrical and radiation certify the x-ray system. The author also facilitated all patient imaging and conducted the preliminary reader study.

CHAPTER 4
Research Aim 2: Creation of the Gs-DCT system

4.1 Introduction

Cystic fibrosis (CF) is a progressive genetic disease that forms mucus build up in the lungs of sufferers, predisposing them to bacterial infections that result in inflammation, scarring, and airway thickening.(O'Connor et al., 2010) Approximately 30,000 people have CF in the United States and 70,000 people worldwide. There is no cure for the disease; the average lifespan of patients approaches 40 years.(Gibson et al., 2003; Stern et al., 2008) The disease affects sufferers from birth, requiring continual vigilance and active therapies to minimize mucus plugging. Disease progression is slowed by treating infection and inflammation as they emerge to limit the damage to the airways.

To follow disease progression in CF, patients are monitored throughout their lifetime starting from infancy, largely using X-ray based imaging modalities. A key study by the Australian Respiratory Early Surveillance team for cystic fibrosis shows the importance of imaging in the early detection and treatment of the disease. (Sly et al., 2013) CF patients are currently followed with chest radiography (CXR) which is low cost and uses a relatively low radiation dose. A typical CXR image requires an effective dose of 0.05-0.07mSv.(Meltzer et al., 2016; Båth et al., 2010)The major limitation of this 2D imaging modality is low sensitivity due to overlapping structures. All chest features such as the airways, lung parenchyma, ribs, and heart are superimposed causing low sensitivity.(Båth et al., 2005; Håkansson et al., 2005) Airway thickening and mucus plugging in CF patients are not well resolved by CXR,(Vult von Steyern et al., 2012) and thus cross sectional imaging may be performed for acute exacerbations.

The main markers of CF severity are well seen on CT. However a significantly higher dose of radiation, between .5 and 3 mSv for adult patients and roughly 1.4 mSv for pediatric patients, is required to obtain a CT scan.(Mott et al., 2013) Due to the long z-axis coverage relative to length of

the thorax, a typical chest CT scan requires a 5 to 10 s breath hold to complete.(Von Steyern et al., 2012)

In order to fill in the gap between the low sensitivity CXR and the high dose high sensitivity CT scan, digital chest tomosynthesis (DCT) has been developed. DCT is a low dose modality that acquires a small number of projections over a limited scanning angle. The images are then reconstructed into a stack of 3D images. DCT requires a long scan time as the X-ray source is translated over the 40° angular span.(Dobbins et al., 2016; Dobbins and Mcadams, 2009)

We have developed a stationary digital chest tomosynthesis (s-DCT) based on the carbon nanotube linear X-ray source array.(Shan et al., 2014b,a) One of the advantages of the carbon nanotube based X-ray source is the ability to perform on demand generation of X-ray pulses. The work presented here depicts the stationary gated digital chest tomosynthesis system that will be tested by performing in-vivo prospectively gated chest imaging utilizing a free-breathing porcine model in chapter 5.

4.2 Materials

4.2.1 System overview

The Gs-DCT system utilizes the s-DCT X-ray source as described in chapter 3. The major changes to the system are the detector, the software that runs the system, the triggering system of the X-ray source, and the BioVet monitoring system. The patient bed has been modified to fit the new detector. The command processor and the controlling computers are in the operators station protected with leaded walls. The driving electronics are in the electronics rack. This section will describe detail the new Gs-DCT imaging system, including system resolution, and physiological monitoring device used in this system.

4.2.2 Detector

The detector used in this experiment is a Varian 4030X amorphous silicon flat panel detector. The detector is driven by a Varian Command Processor. The command processor supplies the power to the detector and transmits images via fiber optic cable from the detector to the command processor. The full scheme of the detector setup is found in figure 4.1 The computer sends commands over an ethernet cable to the command processor to set the mode and frame rate of the detector. The user

communicates the mode of the detector using the ViVA software. The ViVA software has the detector 4 modes preprogrammed and the options for each mode built in. Before image acquisition begins, the user must initialize the detector using ViVA.

The detector has two phases, integration and readout. The integration phase is when X-rays are being counted. The readout phase is when the image is being transmitted to the computer and reseting for the next integration phase. The detector is continuously oscillating between readout and integration. The read out time of the detector is fixed based off of the mode. The integration time is variable by changing the frame rate of the detector.

During the readout time, the images are transmitted from the detector to the command processor. Then, the command processor transmits the images to the computer via camera link cable through a BitFlow frame grabber card. The command processor performs the dead pixel correction before reading out the image. The purpose of the frame grabber card is to wait for images to be transmitted. Then when triggered, the frame grabber card will read in the image into the computer.

The command processor has an external sync port that allows for synchronization between the X-ray source and detector. The external sync pins are a series of 24 pairs of opto-couplers. The difference in voltage between the two pins indicates high or low for the pair. For this application, pins 9 and 10, named Expose_Ok are used. When Expose_Ok is high, the detector is integrating. Pins 7 and 8 are Panel_Healthy, these are read in as an error checking mechanism.

In order to ensure that each X-ray pulse has time to start and finish within an integration phase, the external sync port is used to trigger an acquisition window signal. The acquisition window is FALSE for the entire readout time plus the pulse width of the X-ray pulse and TRUE during the integration phase. This truncation of the signal ensures all pulses are started when the acquisition window is TRUE can be completed in the integration phase.

There are both full resolution and binned modes for this detector. The full resolution detector reads out the value of each pixel which requires 42 ms. The detector can run up to 10 fps in this mode. The binned modes for the detector bin in a 2x2 fashion, meaning 4 pixels are binned together. The binned modes only require 16 ms to read out. Therefore, the detector can be run up to 30 fps. An individual pixel is 0.194mm in each direction so in the binned mode, each pixel is 0.388mm. For the work presented here, the detector is in full resolution mode and run at 5 fps.

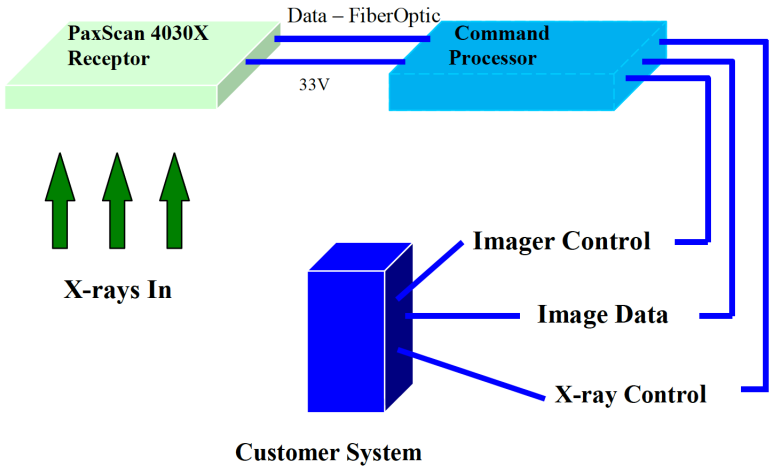

Figure 4.1: The detector connection scheme. The x-rays are input on the flat panel detector and transmitted over a fiber optic cable to the command processor. The command processor supplies power to the detector and transmit data to the customer system. In this case, the customer system is the computer with BitFlow card. The x-ray control interface is ViVa software provided by Varian. (Image from the Varian 4030X detector manual)

4.2.3 System resolution

The resolution of the X-ray system was measured using the modulation transfer function (MTF). First the line spread function (LSF) was measured using a 100μm diameter tungsten cross-wire phantom placed 10.4cm above the detector. The LSF was measured using a slant angle over sampling method.(Tomashefski et al., 1986; Kwan et al., 2007) The LSF was fitted to a Gaussian function to remove noise before doing a Fourier transform. The in-plane resolution was measured as the frequency at 10% of the MTF and was measured in both x and y directions. For this system, the MTF was measured to be 2.83$\pm$0.06 line/mm perpendicular to the scanning direction and 2.11$\pm$0.08 line/mm in the scanning direction, shown in figure 4.2.

4.2.4 Physiological system monitoring

The Bio-Vet system is used to monitor physiological signals. A BioVet system includes electrocardiogram (ECG) leads, pressure sensor, transformers, and command module. As well as a DATAQ Instruments (Model # DI-155, USB data acquisition starter kit) in order to save the physiological data from the BioVet system. The DATAQ is referred to as the BIODAQ because it is the data acquisition module for physiological data. The ECG leads are placed on the subject and provide data on the

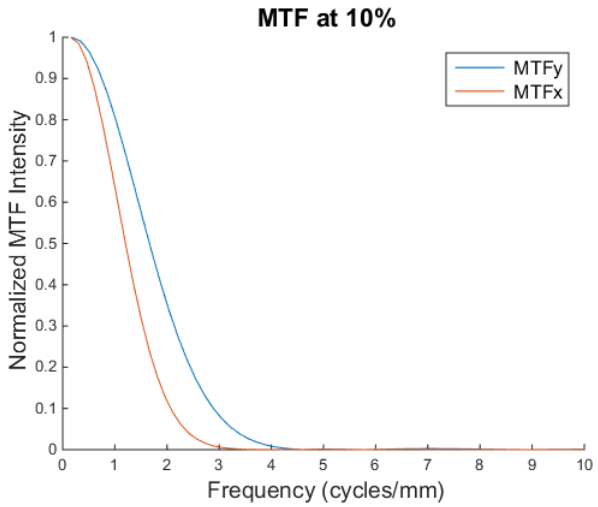

Figure 4.2: The MTF functions for in the scanning and anti-scanning directions. 10% of the MTF was reported as the resolution for the system. The scanning direction is 2.11±0.06 line/mm and perpendicular is 2.83±0.08line/mm

cardiac cycle. For respiratory gated imaging, the ECG signals are not necessary but will be used in future experiments for cardiac gated imaging.

The pressure sensor is attached to a strap that is placed around the abdomen of the subject. This sensor monitors the breath cycle and is known as the RSP signal. The high pressure signal corresponds to the inhalation of the patient where the low pressure signal corresponds to the exhalation phase of the patient.

The raw pressure signal is then sent to a Bio-Vet transformer. The transformers take the raw signals from the ECG and RSP signals and transfers them to the command module. The command module turns the analog signals into digital triggers. Whenever the pressure is above the set threshold, the output trigger is a TTL TRUE signal for the predetermined trigger time. The threshold for the ECG signal can also be set. In that case, the command module would output a dual trigger. In the dual trigger mode, the exhalation phase of the breath is isolated and the R wave is commonly used.

The BIODAQ has 4 ports and records the data from each of these ports during the duration of imaging. The recorded quantities are ECG signal, RSP analog signal, the RSP trigger from command module, and the X-ray triggered signal. The X-ray triggered signal comes from the pulse generator that triggers the MPE. This data is saved in Excel sheets with 10ms time between each data point.

4.3 Results

4.3.1 X-ray triggering system

The X-ray triggering system relies on the temporal coincidence between the detector integration window and the physiological trigger. The most important part of the X-ray trigging system is filtering each of the signals in the system such that each signal is only true when an X-ray pulse has time to start and finish while that signal is still in the desired phase.

The detector signal is filtered to create the acquisition window. Figure 4.3 shows the LabVIEW code for the detector signal filtering. First, the expose_ok detector signal is read in through the DAQ and the edge is isolated. When an edge is detected, an output port on the DAQ is set to true. Then, the time the acquisition window is true (AWT) is calculated using equation:

$$AWT = \frac{1}{fps} \times 100 - BT - PW \tag{4.1}$$

Where fps is the detector speed, fps, the buffer time (BT) is 90ms or 120ms, and PW is the x-ray pulse width. The buffer times are to ensure the acquisition window is aligned with the expose_ok signal. They were found by watching the small shifts in the acquisition window with respect to the signal on an oscilloscope. The shifting between the acquisition window and the expose_ok signal come from the delays in DAQ data transfer and Labviews clock. The buffer time is increased to ensure synchronization between the acquisition window and detector phase at small pulse widths. After the AWT time has passed, the output port is set to false. This logic allows for dynamic acquisition window calculations. Therefore, the system can take scout images to determine the dose for the tomo scan and update the AWT within 1 detector cycle.

The RSP trigger is a pulse of fixed length that is triggered when the pressure on the pressure strap is above a predetermined threshold. The threshold must be high enough to create a tight gating window to ensure that if an X-ray is triggered at the end, will still complete within peak inspiration. In the dual trigger mode, the ECG trigger uses a gating window small enough to isolate the desired cardiac phase. In the dual trigger mode, the BioVet will only output a TRUE physiological trigger if both the ECG and the RSP signals are in the desired cardiac and phase.

This acquisition window and the physiological trigger are fed into a 3 way AND gate. The 3rd port is for the 'imaging on' signal; this is a signal that is TRUE with the user starts the imaging process. This triggering scheme is shown in figure 4.4. The temporal coincidence of the physiological trigger and the acquisition window determines if the X-rays will be triggered. The trigging system is used during the scout image acquisition and the tomosynthesis image acquisition. Figure 4.9 and 4.10 show how the trigging system is used in the larger Gs-DCT system.

4.3.2 Image saving

Saving the detector images requires synchronization between the detector command processor and the frame grabber card. The images are transmitted from the command processor to the frame grabber card. The frame grabber card loads the images into LabVIEW where they are converted from raw files into .tiff files. The images are saved as .tiff files because that is the fastest LabVIEW saving format (determined experimentally). Synchronization between x-ray triggering and image saving is done using a variable name 'X-rayOut', shown in figure 4.5. This variable is true for the 500ms after each x-ray pulse to ensure that all images are read into LabVIEW.

Figure 4.6 shows the LabVIEW module for saving images. First, the BitFlow card is opened, setup, and set to continuously read in images. Then, the file names and paths are created. When an x-ray is triggered and the user is collecting a scout image, then the scout case structure is entered. The first frame saves the image to the predetermined file path. Using the IMAQ vision suite, the image is displayed with controls for the user to select the ROI. The mean of the pixel values in the ROI is then calculated:

$$PW = \frac{ScoutmAs}{mean + 17.184} \times 200,000 \tag{4.2}$$

The ideal imaging pulse width would yield a pixel value of 2/3 the dynamic range in the lung region. Therefore, using the scout image, the pulse width needed to give 2/3 the dynamic range of the detector is calculated. In equation **??**, the Scout mAs is determined by the size of the patient. The mean is the mean pixel value, 17.184 is a correcting factor and 200,000 is a scaling factor. In the next frame, if the calculated pulse width is less than 20ms, the longer buffer time is required and the

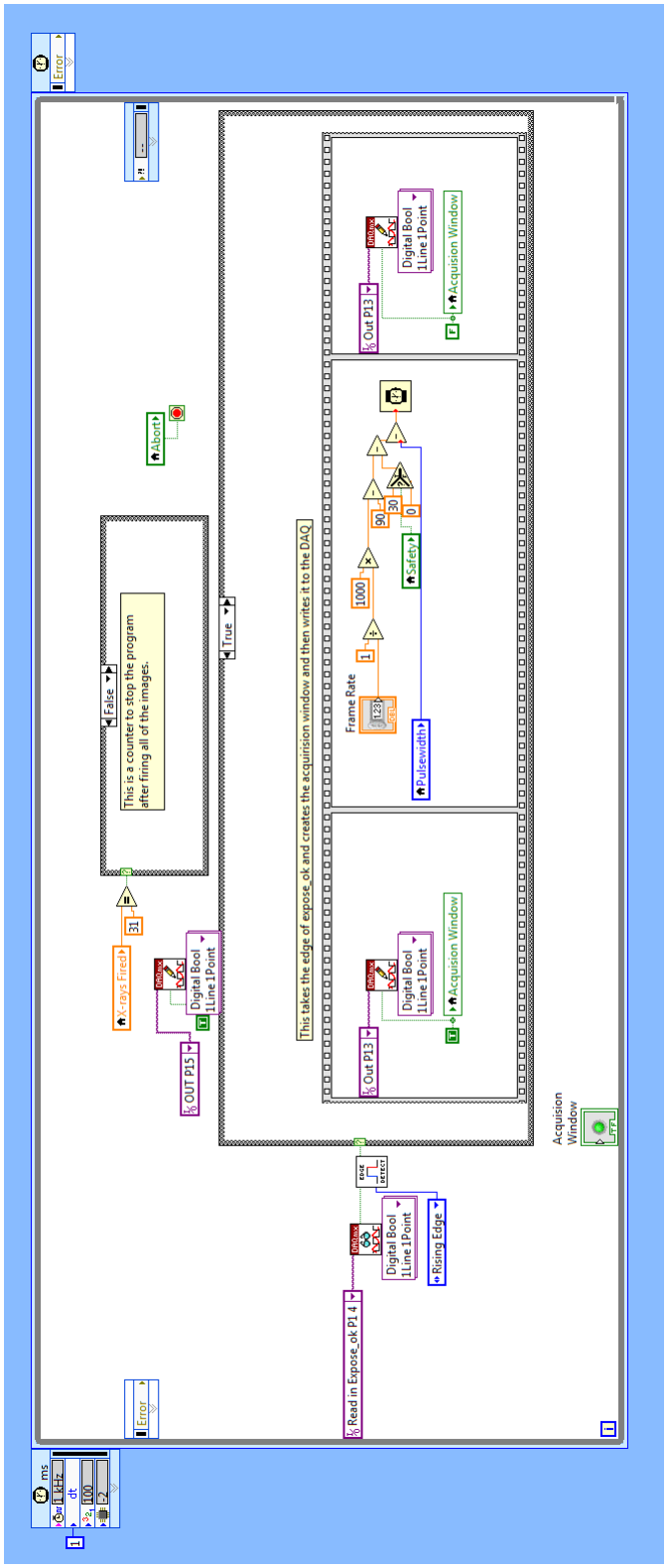

Figure 4.3: The LabVIEW code that creates the acquisition window signal. The acquisition signal is made by a series of pulses. Each pulse is a truncated version of the detector signal.

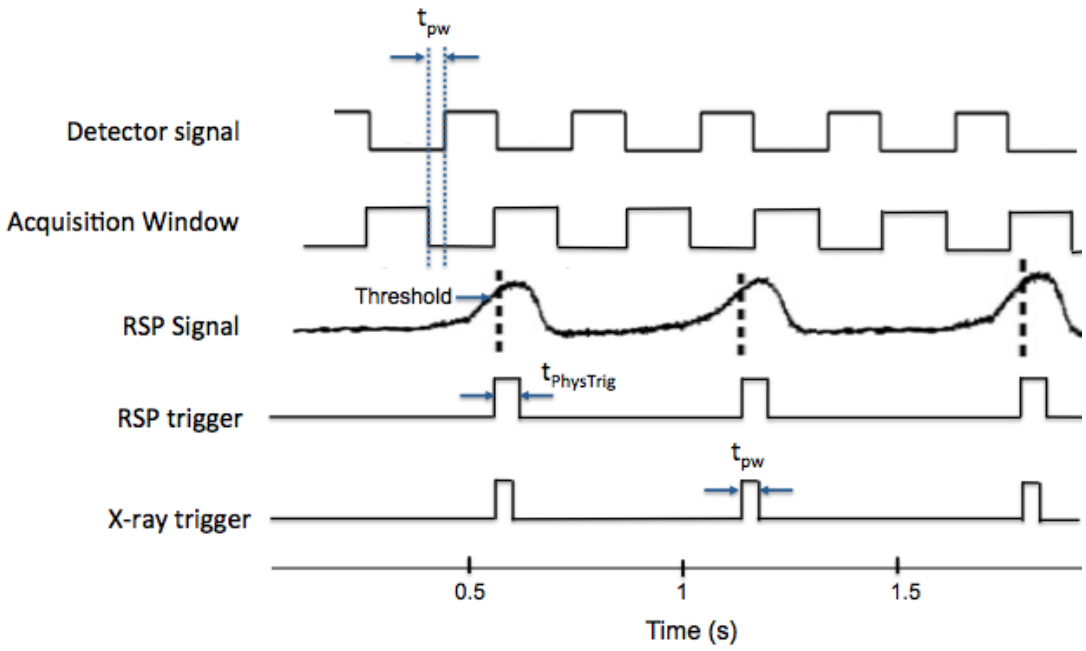

Figure 4.4: Triggering scheme for the Gs-DCT system. This system shows the truncation of the detector signal to create the acquisition signal. The Bio-Vet transformer takes the analog RSP signal and uses a threshold to create the RSP trigger. Then, when there is temporal coincidence between the RSP trigger and acquisition window, an x-ray is fired. Image adapted from (Cao et al., 2010)

safety is turned TRUE. After the pulse width has been calculated, the value is sent to a text file for future reference and all of the other values are re-initialized to default values.

For the tomo imaging, the images are saved using the LabVIEW IMAQ suite when the x-ray trigger is TRUE. After each image is saved, the frame counter is increased by 1. After 29 tomo images, the BitFlow card is stopped, all of the reference numbers are released, and the card is closed.

Images are only saved after an x-ray is fried to Saving the detector images is the current speed limitation in Gs-DCT system. The X-ray images can be triggered and displayed at 10 fps, the fastest setting on the detector in full resolution mode. The saving speed is limited by the transfer of data into and out of LabVIEW.

4.3.3 Logical workflow

The logical workflow of the Gs-DCT system is suitable for clinical operation. The front panel of the LabVIEW program is shown in figure 4.7. This panel shows the Patient ID that is input before imaging. The pulse width for the scout image and an example patient image.

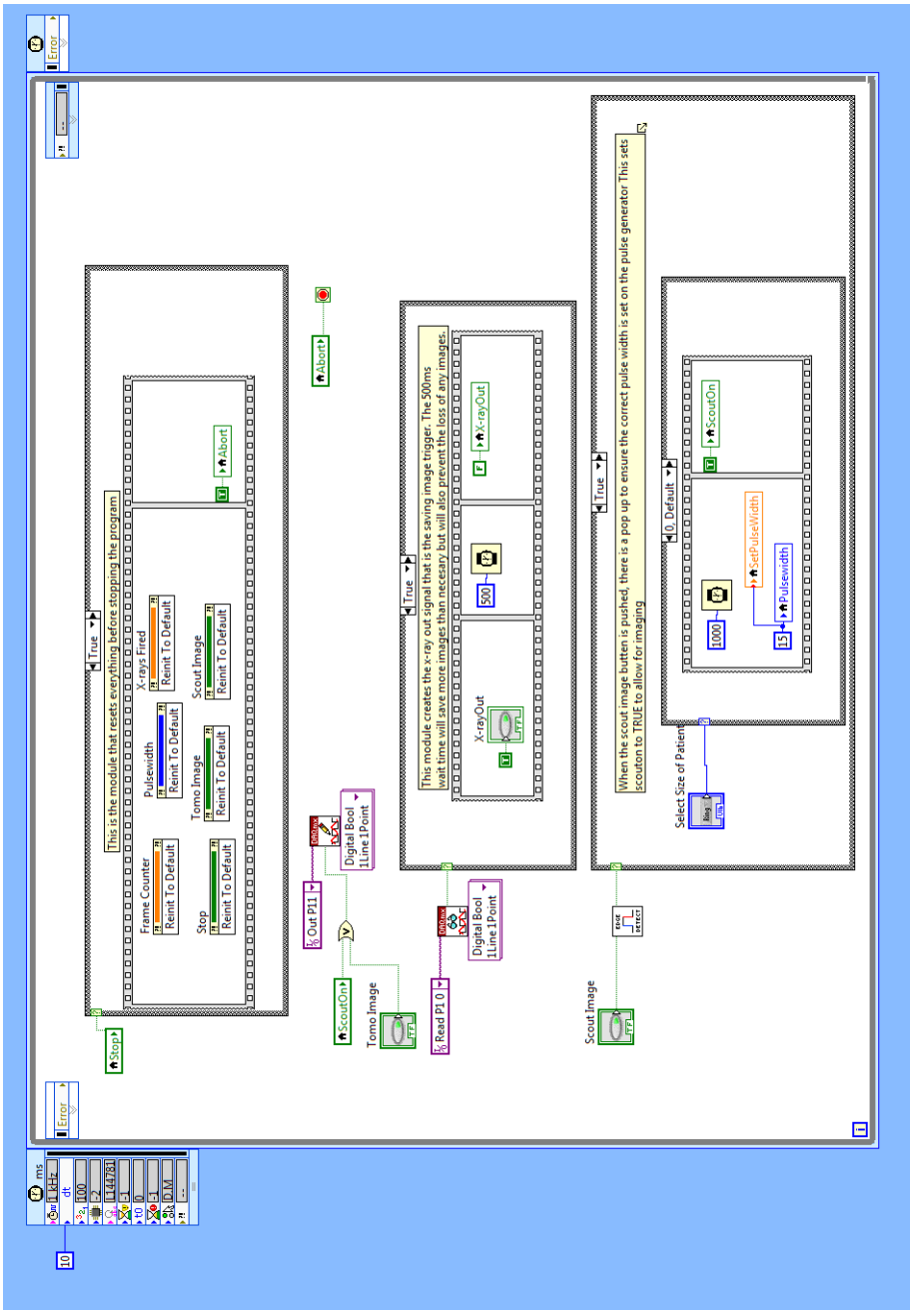

Figure 4.5: This module of LabVIEW code is responsible for system shutdown, image saving synchronization and converting patient size into scout image mAs.

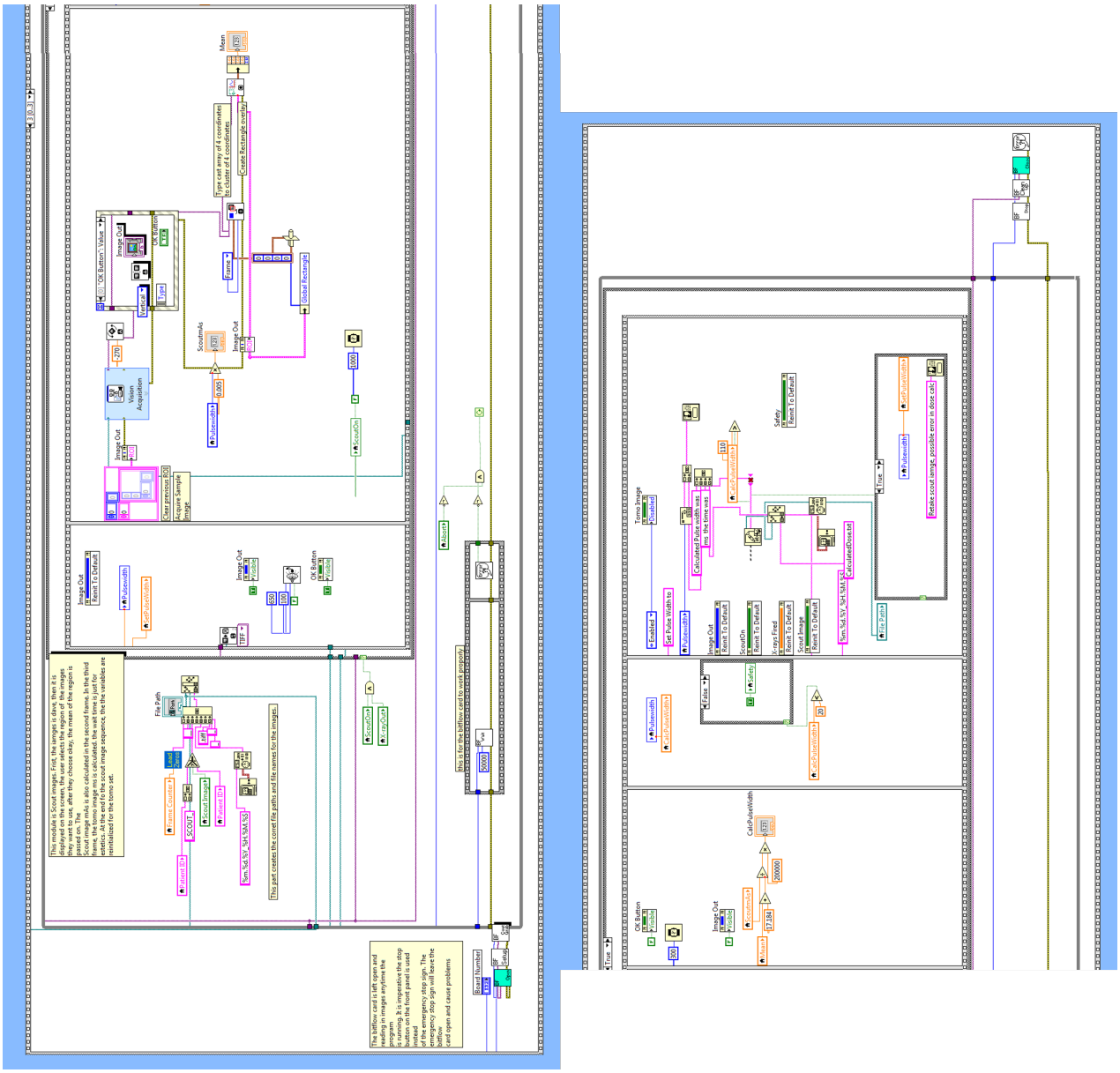

Figure 4.6: This LabVIEW module is responsible for reading in the images from the BitFlow card. There are two cases for reading in images: scout images and tomosynthesis images. For the scout images, the image is displayed and the tomosynthesis pulse width is calculated. For the tomo images, the images are saved to the correct folder and not displayed.

The system logic for the Gs-DCT system is shown in figure 4.8 At the start of imaging, the Bio-Vet computer is setup, the detector is initialized using ViVa, and an ethernet connection is established to the x-ray source. Then, the patient is positioned on the detector and the Bio-Vet sensor is placed on their abdomen. The patient is then checked into the x-ray source and detector computers. This process creates files to store the imaging logs from the x-ray source and the images from the detector. The scout image subroutine is then entered. The scout image is displayed on the screen and the user selects the ROI and the tomo dose is calculated. If the patient is in the correct position, the tomo subroutine is entered. If not, the patient is repositioned, and the scout image is retaken.

The scout image subroutine is found in figure 4.9. The subroutine starts by raising the anode voltage and initializing the MPE to fire the center source one time. The user then switches the 'Imaging On' signal when they are prepared for x-rays. Then, the system waits for temporal coincidence between the physiological signals and the detector. The next image to reach the BitFlow card is saved and displayed on screen. The mean ROI is measured and the pulse width needed for the tomo set is calculated. After the pulse width for the tomo set is calculated, the scout image subroutine is exited.

The tomo logic subroutine is found in figure 4.10. Much like the scout image logic, the subroutine starts by raising the anode and initializing the MPE. In the tomo logic, the MPE is initialized to fire each x-ray source one at a time. When the user is ready to acquire the tomosynthesis images, they turn on the 'Imaging On' signal. The system then waits for temporal coincidence of the physiological signal and the detector signal. When there is temporal coincidence, a single x-ray source is fired. The next image to reach the BitFlow card is saved. Then, the system checks the number of x-rays fired. If the imaging sequence is not complete, then the system again waits for temporal coincidence. If the system is complete, the anode is lowered and the system shuts down.

The shut down sequence for the system can be seen in figure 4.5. The case structure at the top of the figure shows the re-initialization of the system parameters and then finally stopping all loops by turning the abort variable to TRUE.

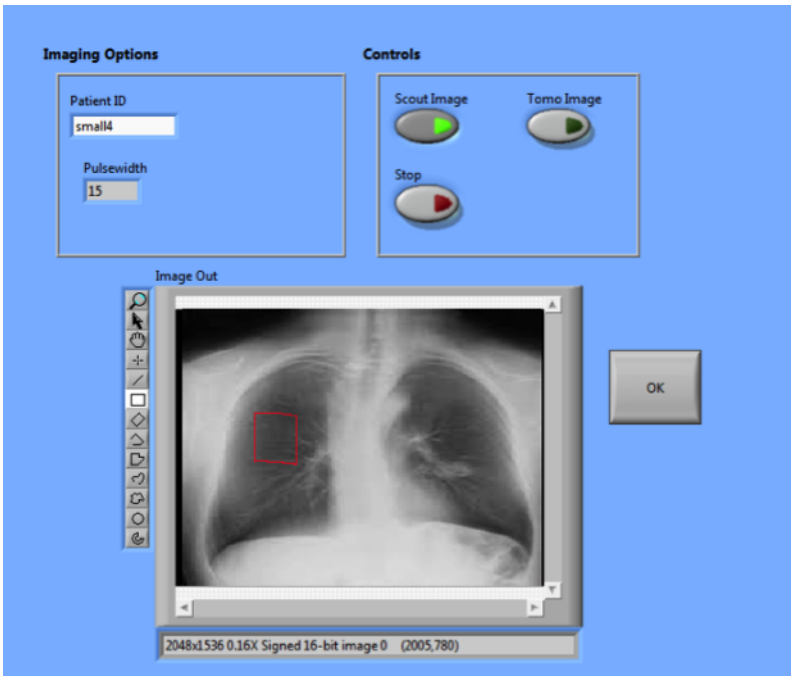

Figure 4.7: The front panel to the Gs-DCT system software.

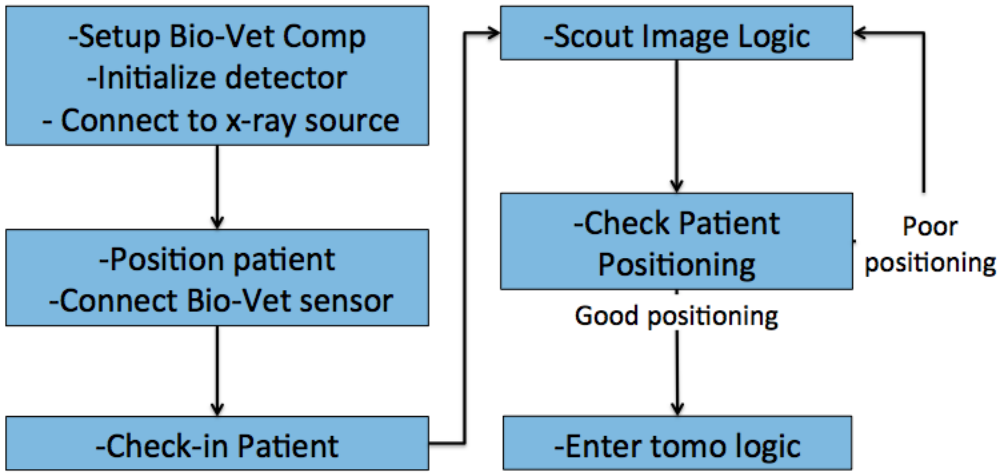

Figure 4.8: The main logic for the Gs-DCT system. First, the signals are initiated by setting up the Bio-Vet computer, initializing the detector, and establishing a connection to the x-ray source. Then the patient is positioned and the Bio-Vet sensor is attached. After the patient is checked-in, the scout image subroutine logic is entered. The patient position is then checked. Finally the tomo subroutine logic is entered.

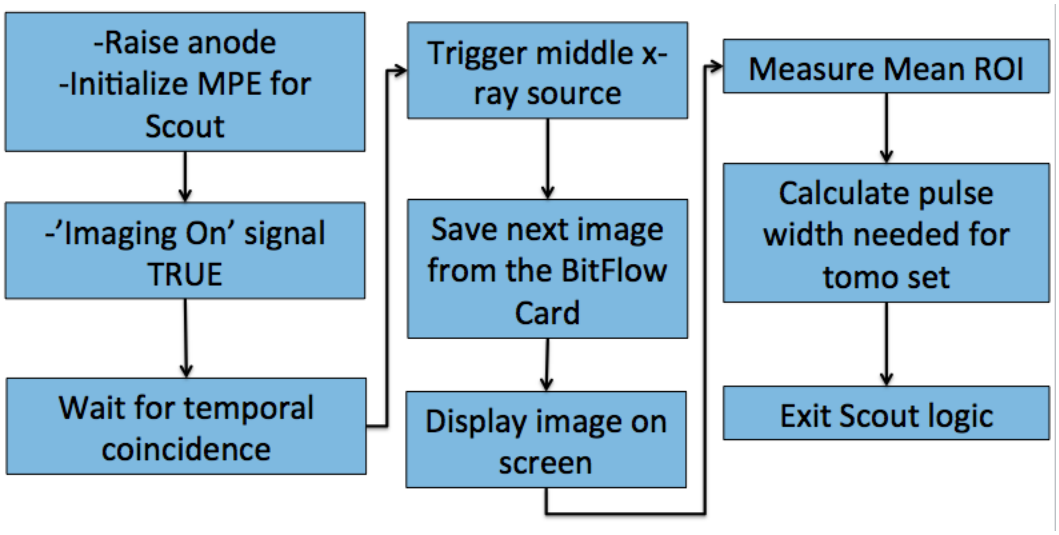

Figure 4.9: The scout image subroutine is presented here. First, the anode is raised and the MPE is initialized. Then, when the user is ready for patient imaging, the user turns 'imaging on' TRUE. Then, the signals are read into the AND gate. The middle x-ray source is triggered when there is temporal coincidence. The next image on the BitFlow card is saved. The image is displayed for the user to select the region of interest. The mean ROI is measured and the pulse width needed for the tomo set it calculated.

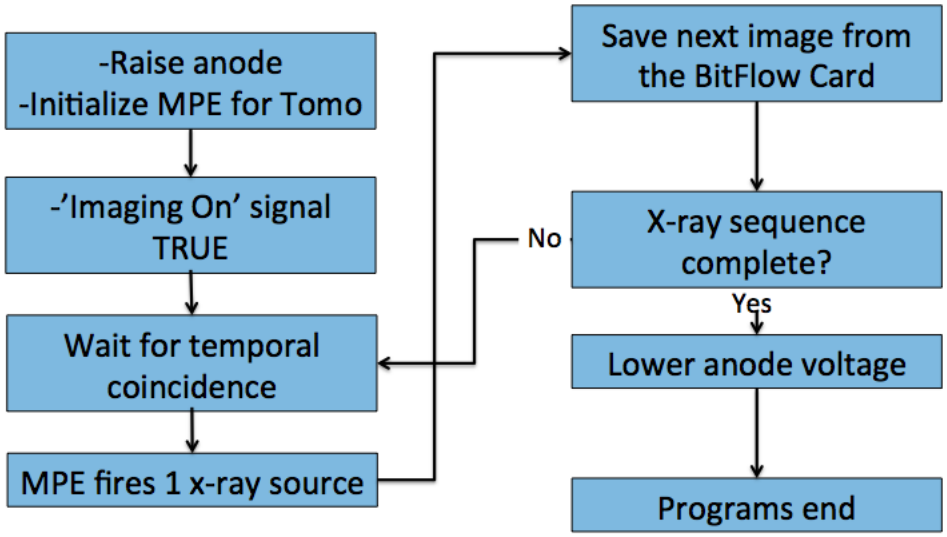

Figure 4.10: In the tomo logic, the anode is raised and the MPE is initialized to fire each x-ray source one time. The user then turns the 'imaging on' TRUE. Then, the MPE fires one x-ray source at the temporal coincidence of all of the signals. After each x-ray source is triggered, the next image to reach the BitFlow card is saved. This is repeated until all 29 sources have been triggered. Then, the anode is lowered and the program ends.

4.4 Conclusions

In the course of the work presented here, a dynamic x-ray triggering system was created. This system adapts to changing pulse widths to allow for patient imaging. The software has a front panel that an x-ray technician can use easily. This system is radiation and electrical safety certified.

CHAPTER 5
Research Aim 3: Quantify the benefit the Gs-DCT system

5.1 Introduction

A dynamic x-ray imaging system was developed. The goal of this chapter is to quantify the benefit of the Gs-DCT system. This was done by using the Gs-DCT system in a free breathing pig study under different imaging configurations. This work is done to evaluate the feasibility of gated patient imaging.

5.2 Methods

5.2.1 Imaging

For this study, a free breathing 5-week-old-pig was sedated and placed supine on the detector. The pig was monitored using the BioVet monitoring system. A pressure sensor was placed around the abdomen of the pig to measure the respiratory motion. The BioVet creates a RSP trigger of predetermined length of time whenever the pressure on the sensor is above a predetermined threshold. For the inspiration experiment, the trigger time was 75ms or 150ms but in patient imaging it can be adjusted in real time.

5.2.2 Image analysis

In order to find the synchronization of the X-ray trigger and the breath cycle, the correlation coefficient between the breath captured by each X-ray pulse and the average breath captured by the scan was found. An image of the calculation is shown in figure 5.1. First, the time the x-ray was triggered was found on the RSP trace. This is shown in step one of figure 5.1. The blue line represents the RSP trace, which was the pressure on the chest strap over time. The vertical line was the time the X-ray was triggered. In step two, a snippet of the breath was isolated by taking the RSP trace signal .5s before the x-ray pulse and .5s after the x-ray pulse. This yields a breath snippet that

represents the breath captured in that x-ray pulse. There are 29 snippets because there were 29 X-ray pulses. In step 3, the pressure value at each time point of the individual RSP trace snippet is average together. This creates an average breath, shown in step 4. In step 4, the average breath is shown in blue and the standard deviation between each point across all 29 x-ray pulses is in red.

After the average breath was calculated, the correlation coefficient between the average breath and each individual breath snippet was measured. This correlation coefficient for each breath was a measure of the motion of the diaphragm between each projection. A large correlation indicates less motion between projections.

Image degradation associated with respiratory motion blur can be quantified by analyzing the diaphragm edge reproduction. During normal breathing, the diaphragm motion is primarily in the plane of the detector (the x-y plane), where the resolution is greatest. In order to quantify the thickness of the diaphragm edge, 5 line profiles were taken on the right side of the diaphragm. The length of each line profile was 25 pixels long. All line profile locations were chosen to be where the diaphragm was most horizontal. This was done to minimize the contrast reduction due to measuring line profiles diagonally across pixels. The line profiles were put through a 3 point moving mean average filter to smooth the profile. Then, the half width at half max (HWHM) was taken of the line profile. This was taken as the edge thickness of the diaphragm. The average edge thickness across all five line profiles was reported as the edge thickness for that scan. The standard deviation of the 5 points was taken to be the error in that measurement.

The blurring of the images was calculated by taking the HWHM of the diaphragm edge in the center projection image before reconstruction. The percent reduction in blurring taken by subtracting the blur in the un-gated image from the blur in the gated image and then dividing by the size of the diaphragm edge in the un-gated image. This calculation can be seen in equation 5.1.

$$\text{Reduction in bluring}(\%) = \frac{(\text{RET}_1 - \text{PET}) - (\text{RET}_2 - \text{PET})}{\text{RET}_1} \times 100 \tag{5.1}$$

Where RET is the reconstructed edge thickness and PET is the projection edge thickness.

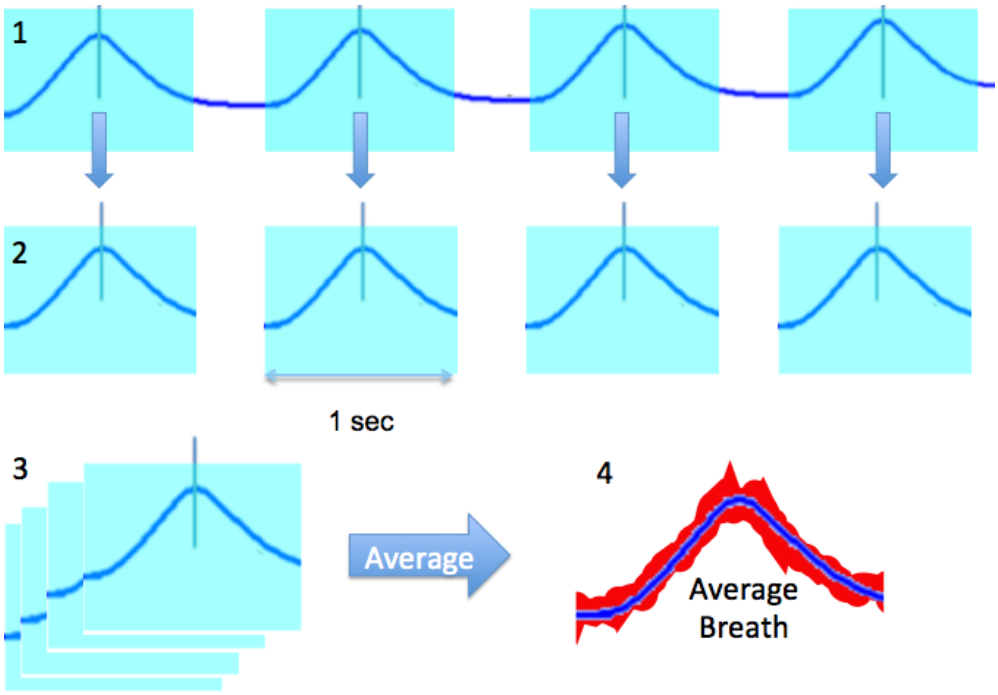

Figure 5.1: Step 1.Blue line is the pressure on the chest strap, this is graphed to create the RSP trace. The x-ray pulse is overlaid (vertical line) and shows where the x-ray pulse was fired during the breath. Step 2. The teal box represents the .5s before the x-ray pulse and the .5s after the pulse. This is used to create a snippet of the breath captured during the breath cycle. Since there were 29 x-rays fired, 29 breath snippets are made. Step 3.The snippets of breath are overlaid, the pressure value of each time point is average together, this creates an average breath, shown in Step 4. The blue shows the average breath captured by the x-ray pulse during the scan. The red shows the standard deviation of the RSP traces through the breaths.

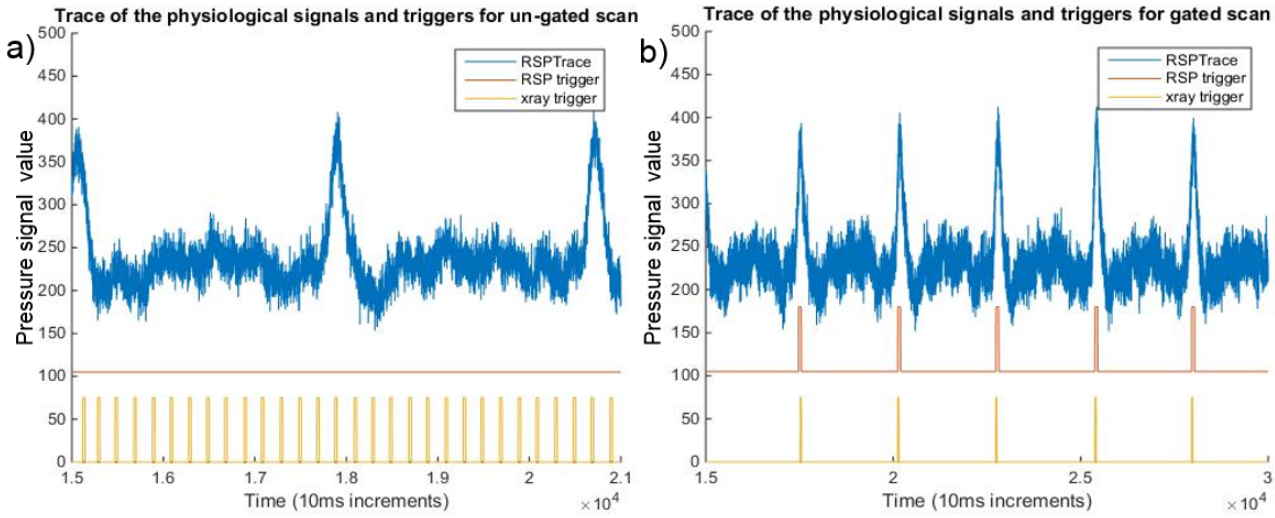

Figure 5.2: (a) The RSP trigger (red) is fixed in the TRUE position for the un-gated study. Therefore, the X-ray triggers (yellow) in every detector acquisition window (not shown) regardless of the breath phase (blue). (b) The X-rays are only triggered when the RSP trigger is TRUE and therefore isolating the peak

5.3 Results

5.3.1 Imaging

In this study, the average breath rate was 24.3±3.5 bpm and the average heart rate was 118.4±2.3 bpm. Eleven un-gated, 5 inspiration gated and 8 expiration gated image sets were successfully completed during this experiment. The total average imaging time for the un-gated study was 6.3±0.6s. For the inspiration gated study, a single frame was taken during each breath cycle yielding a total imaging time of 81.7±11.9s. The entrance dose used in this experiment was 0.4mSv.

The physiological signals and trigger were recorded and are shown in figure 5.2. Figure 5.2(a) shows the signal map from the un-gated scan. In the un-gated scan, the respiratory trigger was high for the duration of the scan. This allowed the X-rays to be triggered by the acquisition window signal. As a result, the X-rays were fired in consecutive detector signals, like conventional tomosynthesis scanning. The respiratory trace, in blue, shows that the projection images were taken over the course of two breaths. The inspiration gated scan is shown in figure 5.2(b). A subset of the X-ray triggers can be seen, a total of 29 breaths were used to acquire the image set. The respiratory trigger is high only when the respiratory trace is above a set threshold. For this trial, one X-ray was triggered for each peak inspiration, this minimizes the respiratory motion between projections.

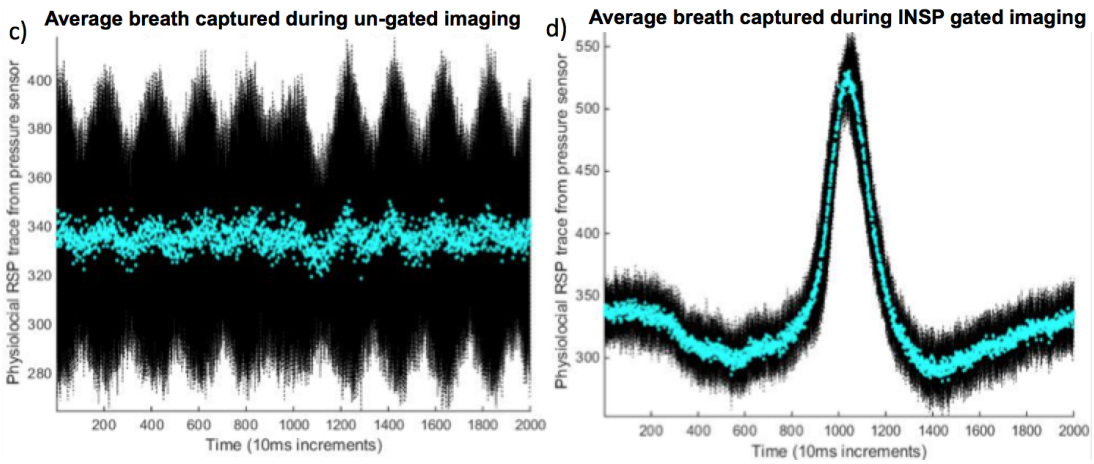

Figure 5.3: a) The average breath signal captured by the X-ray trigger in the un-gated imaging setup (blue) the black is the standard deviation of the average at each point. There is an average of 0.12± 0.02 correlation between the average breath captured and each individual breath captured. b) The average breath captured by the X-ray trigger in the RSP gated study (blue). The standard deviation of the average is shown in black. The correlation between each breath captured is 0.91 ± 0.06.

5.3.2 Breath correlation

The average correlation for each image set was found between the average breath signal and the breath of each projection for each of the studies. Figure 5.3(a) shows the average breath signal (blue) and the standard deviation of that breath in black for an image captured in the inspiration phase. Figure 5.3(b) shows the correlation graph for the gated case.

A between-subjects, one-way analysis of variance (ANOVA) was calculated to determine if differences in correlation coefficient existed for gated and un-gated scans. The overall model was significant, $F(2,691) = 431.353$, $p<0.001$, partial eta = 0.556. To determine which groups significantly differed, post hoc comparisons using Tukey HSD test indicated that the mean score of un-gated correlation coefficient (M =0.12, SD = 0.20) was significantly different than the RSP gated case (M = .91, SD= 0.06) . The un-gated scan showed significantly different correlation coefficient than the RSP gated (M = 0.66, SD = 0.04, $p< 0.001$).

5.3.3 Image quality

The reconstruction of the diaphragm is shown in figure 5.4. The un-gated reconstruction of the diaphragm is shown in figure 5.4(a). This image shows blurring and contrast degradation at the diaphragm edge. The gated reconstructed diaphragm is shown in figure 5.4(b) where no significant

signs of image degradation due to respiratory motion can be seen. Figure 5.4(c) is the line profile of the diaphragm edges for both the gated and un-gated studies. The average HWHM of the un-gated diaphragm edge is 2.6 $\pm$ 0.6 mm and 1.8 $\pm$ 0.5 mm for the gated study. The projection image diaphragm edge is a measure of the diaphragm edge with no blurring due to motion. In this case, the projection image diaphragm edge was 0.7 $\pm$ 0.1mm.

5.4 Discussion and conclusion

5.4.1 Physiological

Overall, the pig remained stable throughout the imaging presented here. There was limited global motion blur due to the sedation of the pig. The breath rate of roughly 24bpm by the pig is similar to an average child. The average breath rate range for an 8-year-old is between 11bpm and 20bpm. Therefore this experiment is a good model for pediatric imaging.

5.4.2 Image Quality

Keall et al., 2006 showed that the lung tumor motion trajectory during a breath cycle is largely in the x-y plane with minimal motion in the z-plane. Therefore, looking at diaphragm motion as a measure of motion blurring is a good assessment of respiratory motion blur in the reconstructed images.

The diaphragm edge was measured using the HWHM of the line profile in the vertical direction across the diaphragm edge. In order to limit the effect of noise on this measurement, a 3 point moving average filter was used. It is common to use a Gaussian fit of the line profile to measure the width of an edge. The diaphragm edge in this case did not have a good Gaussian fit, therefore the HWHM of the Gaussian fit was not an accurate representation of the diaphragm edge thickness. For this reason, a smoothed line profile without fitting was used.

There was up to a 52% reduction in blurring of the diaphragm in the inspiration-gated case compared to the un-gated case. The diaphragm shows the greatest motion so it has greatest potential benefit from gating; more subtly, the reproduction of the vasculature in the lungs was also improved by gating. The reproduction of the vasculature was improved partially because of the reduction in reconstruction artifacts induced by the motion. These are horizontal line artifacts in the reconstruction,

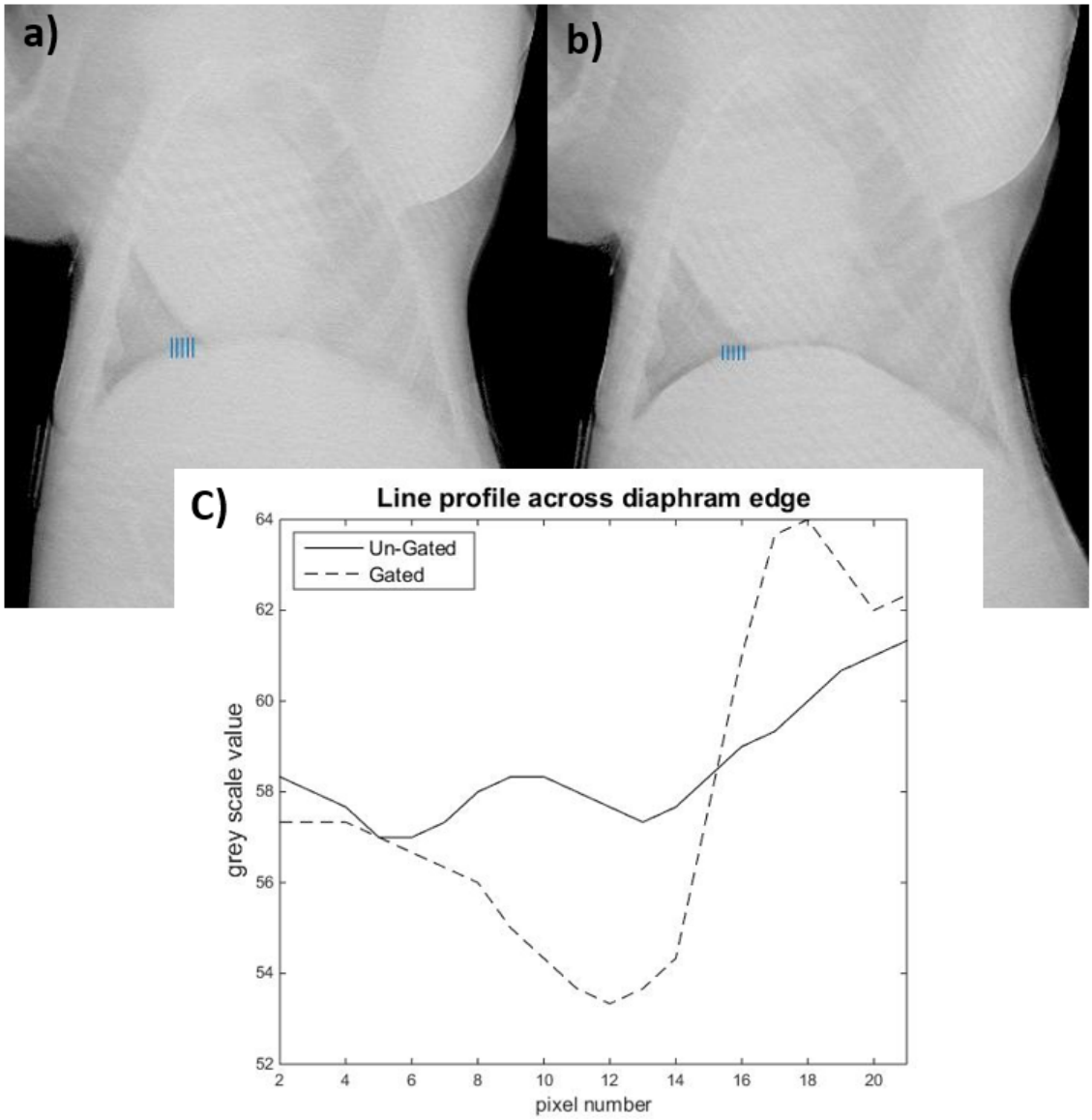

Figure 5.4: A slice of the reconstructed image set where the diaphragm is in focus a) The diaphragm is blurred due to the motion during the projection images. The HWHM of the diaphragm edge is 2.6$\pm$0.6mm. b) The diaphragm edge is sharp due to the minimal motion during projection images, the HWHM of the edge is 1.8 $\pm$0.5mm. c) A line plot over the diaphragm edge showing that the gated study has a significantly higher contrast than the un-gated study.

this is due to the change in position of the diaphragm through each iteration of the reconstruction algorithm.

The bench top s-DCT system used a dynamic phantom in a proof of concept gating study.(Shan et al., 2015a) This study used intubated porcine lungs in a hollow chest phantom as a dynamic phantom. The pressure sensor was placed between the lung and the chest wall to measure the breath phase of the lung. During this experiment, 31 X-ray projections were acquired with no mechanical motion of the phantom, source, or detector. The detector was run in a low-resolution 10fps mode. The movement of a 2mm metal bead was measured during a prospective gated s-DCT scan. This study used a 500ms physiological trigger time and ran the phantom at 10bpm. This proof of concept study showed 85.7% reduction in the respiratory motion blur in the gated study vs. the un-gated study.

The proof of concept gating study found a larger reduction in motion blur than the study presented here. That is largely due to the dynamic phantom used in the study. The displacement of the metal bead in a dynamic phantom was greater than the small displacement in the pig chest in this study. Therefore, the motion in the control images was exaggerated as compared to an *in-vivo* model.

Global motion during a scan is a component of image quality that will need to be examined during human imaging. Global motion could be seen by looking at the blurring of the posterior ribs in the reconstructed images. Further testing needs to be done on global patient motion blur during these longer scans. The average inspiration scan time was roughly 82s. Due to the long scan times of MRI, roughly $7 \sim 16$m, the 82s scan time should be well managed. (Dournes et al., 2016). The inspiration gating was taken in optimal conditions with one frame taken per breath. In order to reduce scan times, the physiological triggers can be relaxed to allow for 2 frames per breath. The impact of this on the image quality will need to be addressed in future studies.

There was a relationship between the correlation of the breaths and the diaphragm edge reproduction, this relationship is dependent on the phase of breath that was isolated during imaging. Using a real time correlation coefficient calculation could be a reliable way to determine the triggering window based off of different breath rates and abnormal breathing patterns.

There was limited global motion blur due to the sedation of the pig but will need to be examined during human imaging. This effect can be seen by looking at the blurring of the posterior ribs in the

reconstructed images. Further testing needs to be done on global patient motion blur during longer scans.

5.4.3 Correlation

The breath cycle was captured using a pressure sensor fixed to the abdomen of the pig. The RSP signal is the pressure on the strap during the breath cycle. Therefore, the correlation between the position of the abdomen in each breath cycle and the average breath cycle centered on the X-ray trigger is a measure of the motion isolation of the system. A high correlation between each of the breath cycles would indicate the abdomen was in the same position during each of the projection images. This eliminates the respiratory motion blur that is a leading cause of image degradation. In order to increase the correlation in the gating case, a smaller gating window could be used. This would limit the acceptable motion during the projection images.

In order to improve the quality of image reconstruction, projection images acquired with a significantly lower correlation coefficient than the average could be removed from the reconstruction. This would reduce the blur in the reconstruction and could improve image quality. An example of this can be seen in figure 5.5. When the physiological trigger is long, there are projections that are taken at significantly lower correlation with the respect to the rest of the scan. Looking at the INSP gated 150ms trigger case, figure 5.5, projections 2, 6 and 9 could be removed. When the projections were removed, the average scan correlation was increased from 0.85 ± 0.11 to 0.87 ± 0.11. As a result, the diaphragm measurement was reduced from 1.82 ± 0.47 mm to 1.57 ± 0.47 mm. The smaller number of projection images may introduce image artifacts. More work needs to be done to analyze the dependence of removing low correlation projections on the reconstructed image sets.

5.4.4 Exhalation gating

Exhalation gated imaging would allow for shorter scan times during cardiac imaging using the Gs-DCT system. There is a plateau during the expiration phase that will allow for the acquisition of multiple heart beats during a single breath cycle. This could keep scan times reasonable while reducing image degradation due to respiratory motion blur.

There was more variation in the correlation coefficients for the exhalation phase compared to the inhalation phase. This was due to the longer trigger times used for the exhalation phase and the

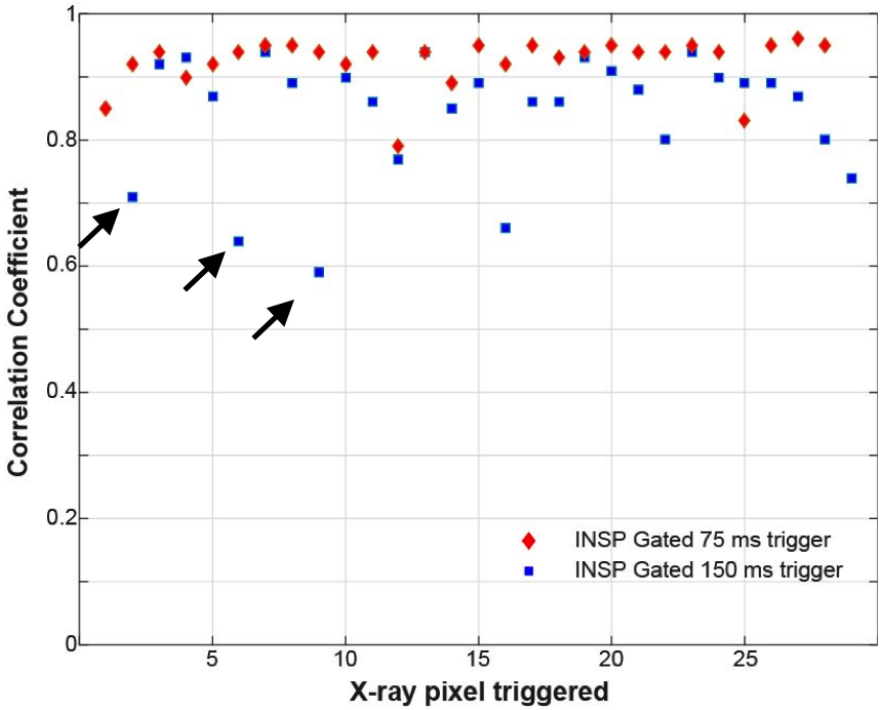

Figure 5.5: The correlation of each projection throughout the image sequence over two physiological trigger lengths. By removing the three points with arrows, the diaphragm edge thickness was reduced from 1.82 ± 0.47 to 1.57 ± 0.47.

higher noise in the physiological signals during the expiration phase. A tighter strap or less noisy respiration-monitoring device may be needed to increase the accuracy of expiration gating.

For the reproduction of the diaphragm in the exhalation cases, there is a 37.8% reduction in diaphragm blurring. This is comparable to previous findings where there was a 36% reduction in the normalized cross correlation of pixel values between pairs of adjacent axial slides as compared to free breathing scans.(Pollock et al., 2016) Therefore, the exhalation-gating scheme presented here, may produce cardiac images with diagnostically relevant quality.

Exhalation cardiac gated imaging was completed using a CNT X-ray source in the micro-computed tomography (micro-CT) scanner.(Burk et al., 2011; Cao et al., 2008, 2010) Due to the low temporal coincidence between the cardiac and respiratory physiological triggers, the detector was set to 1fps. This increases the rate of temporal coincidence of the physiological signals and detector integration time. The triggering system relied on the physiological sensor connected to the mouse. The physiological sensor collected both ECG and RSP signals. Then, when the detector, the ECG, and the RSP signals were all in the correct phase, an X-ray was triggered. This trigger allows for real

time prospective gating. This triggering system was able to successfully image 10 mice with a breath rate of 101bpm and a heart rate of 418bmp. This system was able to obtain high quality images of heart ventricles in a free breathing mouse. The triggering scheme presented in this study was adapted to create the Gs-DCT triggering scheme. The triggering and timing of this system were scaled and adapted to allow for human physiological signal speeds.

Kim et al., 2014 showed that video feedback could increase the between breath diaphragm position consistency. Due to the higher quality of inspiration gated imaging, further testing should quantify the benefit of using a quasi-breath hold technique for patients able to follow breath commands during cardiac imaging. If exhalation gating does not provide enough consistency between breaths, there are semi breath hold techniques using a video feedback spirometer that has been used to guide children through breath holds to increase CT quality. Salamon et al.,2016 This study found that a key component for video feedback to decrease motion blur is training of the patient to follow the breath commands. For young pediatric patients, this is not a viable option.

Free breathing scans have also been evaluated as a CF screening tool.(Saguintaah et al., 2017) This free breathing study showed that air trapping in the lungs could be seen and used to differentiate healthy patients from CF patients but the rest of lung indications were not well viewed.

5.4.5 Previous work done on gated chest imaging

Predictive cardiac and respiratory gating has been developed and cardiac gating is used clinically. Predictive cardiac gating utilizes previous cardiac cycles to predict when the heart will be in the desired phase. Then, the X-ray trigger time is predicted and sent to the imaging source. The predictive trigger is needed due to the low temporal resolution of the system.

This predictive cardiac trigger is in clinical use; the patient is asked to hold their breath while the CT acquires images of the heart during the desired phase. The cardiac cycle is highly regular and after a rhythm has been established, the time of the desired cardiac phase is easily predicable. The images are taken in a single breath hold during multiple cardiac cycles. This cannot be completed on patients with a heart rate faster than 90bpm or on patients who cannot complete a 10 second breath hold.(Desjardins and Kazerooni, 2004) Retrospective gating is used for patients who do not qualify for predictive gating. Retrospective gating acquires a CT scan over many cardiac cycles and then

during the reconstruction process, the projections are filtered by the cardiac phase in which they were acquired.

Using a similar predictive gating technique, (Lell et al., 2016) created a respiratory gated imaging trial. In this experiment, a high pitch dual source CT was taken in a single breath cycle. A near peak inspiration threshold was found during 3 breath cycles. When the threshold was reached on the 4th breath, an entire CT scan was taken in .85s. For this experiment, patients were breathing at an average rate of 4bpm. Therefore, the images were taken during 8.5% of the breath cycle yielding minimal respiratory motion during the scan.

This predictive trigger is adequate for some patient populations and some indications such as patients with good breath control. The Gs-DCT system presented is a more flexible system that can image a large range of patient populations with a reduced dose of radiation.

5.5 Limitations

The limitations on the Gs-DCT system are the short length of the X-ray tube and the low X-ray flux. The short length of the X-ray tube limits the depth resolution of the system. The low X-ray flux limits the temporal resolution of the system. With a higher X-ray flux, the length of each pulse width could be decreased. Decreasing the pulse width would reduce the motion blurring in each projection image and increase the temporal resolution of the system.

An inherent limitation of gated imaging is the long scan time. This study was not able to evaluate the effect of global patient motion blur on image degradation due to the sedation of the pig during imaging. This will need to be evaluated in future studies.

5.6 Conclusions and future work

This Gs-DCT system can effectively gate to RSP and ECG signals. The correlation coefficients can be used to assess the motion between projection images. The image blur can be reduced by 52% using the gated triggering system.

In conclusion, the Gs-DCT system successfully reduced image degradation due to respiratory motion in a free breathing pig using prospective gated imaging. This multi-pixel X-ray source and prospective triggering system will allow for patient imaging in populations that cannot complete a breath hold. This triggering system can also be applied to dual trigger cardiac gated imaging.

In further testing, the largest acceptable window for inhalation and exhalation studies should be found to ensure the shortest possible scan times. A key component of this will be to determine the lowest correlation coefficient that yields diagnostically relevant images. There will need to be some optimization between the respiratory motion blur and global patient motion blur by optimizing the physiological trigger length and the total scan time. This will be apparent during patient imaging.

Pediatric CT and calcium scoring clinical trials are planned. In the future, the system could be modified to allow for real-time correlation coefficient calculations that would allow for images to only be acquired in breaths with a high correlation coefficient or allow for images with lower correlation coefficients to be retaken during imaging. Future studies will explore prospective gated cardiac imaging.

CHAPTER 6
Summary and Future Directions

6.1 Summary

A gated stationary digital chest tomosynthesis system prototype has been developed using a CNT X-ray source array. The key components of this system include a multi-pixel X-ray source array, a flat panel detector, and a sophisticated triggering system. This system is now undergoing clinical trials for use in pediatric patients with CF.

Key research aims discussed in this study include the optimal image protocols for gated patient imaging, the feasibility of a gated chest tomosynthesis system, and the benefit of the a gated chest tomosynthesis system. It was shown that the frame rate of 5fps in this system is adequate for physiologically relevant imaging. The system created successfully gated to a young pig and could handle all irregularities in the breath cycle during imaging. For patients not capable of a breath hold, the Gs-DCT system has been shown to significantly improve the image quality. This reduces the need for pediatric patients to be sedated and intubated for CF disease analysis.

This system is currently installed in Marsico Hall for clinical evaluation. The system successfully passed electrical and radiation safety tests. The clinical trial has been approved by the Institutional Review Board (IRB) at UNC.

6.2 Future Directions

This system could potentially allow for for significant improvements to imaging impacted by respiratory motion blur. This system could allow for free breathing, low dose calcium scoring for screening of heart disease. This could give doctors better information on potential heart conditions in patients with fast heart beats or patients not capable of a breath hold.

This triggering system could be adapted to an X-ray source array with a larger scanning angle or higher flux. The larger scanning angle would increase the depth resolution of the system and allow

for screening of lung nodules without requiring a breath hold. The higher X-ray flux could allow for faster projection acquisition times and increase the quality of gating.

Though there will be a limited impact on gated scan times, the detector could be made to run at 10fps with a more sophisticated image saving system. With a faster detector frame rate, rapid non-gated imaging could be possible. This would allow for a complete tomosynthesis scan to be acquired in approximately 3 seconds.

Creating a portable gated chest tomosynthesis system could allow for gated chest images on trauma patients. This could provide valuable feedback to doctors in the emergency room setting for patients that cannot be moved.

BIBLIOGRAPHY

(2013). US Food and Drug Performance standards for ionizing radiation emitting products. Technical report, US Food and Drug Administration, Silver Spring, MD.

(2014). Lung CT Screening Reporting and Data System (Lung-RADSł).

Båth, M., Håkansson, M., Börjesson, S., Hoeschen, C., Tischenko, O., Kheddache, S., Vikgren, J., and Månsson, L. G. (2005). Nodule detection in digital chest radiography: Effect of anatomical noise. *Radiation Protection Dosimetry*, 114(1-3):109–113.

Båth, M., Svalkvist, A., von Wrangel, A., Rismyhr-Olsson, H., and Cederblad, A. (2010). Effective dose to patients from chest examinations with tomosynthesis. *Radiation protection dosimetry*, 139(1-3):153–158.

Behlig, R. (2016). *Modern Diagnostic X-ray Sources*. CRC Press, New York.

Bertolaccini, L., Viti, A., and Terzi, A. (2015). Digital tomosynthesis in lung cancer : state of the art. *Ann Transl Med*, 3(10):4–7.

Burk, L. M., Lee, Y. Z., Heathcote, S., Wang, K.-h., Kim, W. Y., Lu, J., and Zhou, O. (2011). Carbon Nanotube Based Respiratory Gated Micro-CT Imaging of a Murine Model of Lung Tumors with Optical Imaging Correlation. *Medical Imaging 2011: Biomedical Applications in Molecular, Structural, and Functional Imaging*, 7965(919):79651L.

Burk, L. M., Lee, Y. Z., Wait, J. M., Lu, J., and Zhou, O. Z. (2012). Non-contact respiration monitoring for in-vivo murine micro computed tomography: characterization and imaging applications. *Physics in medicine and biology*, 57(18):5749–63.

Bushberg, Jerrold T. , Seibert, J. Anthony, Leidholdt, Edwin Jr, Boone, J. M. (2002). *The essential physics of medical imaging*.

Calliste, J., Tucker, A. W., Gidcumb, E., Kuzmiak, C. M., Lu, J., Zhou, O. Z., and Lee, Y. Z. (2015). Initial clinical evaluation of stationary digital breast tomosynthesis. *SPIE Medical Imaging: Physics of Medical Imaging*, 9412:941228.

Cao, G., Burk, L. M., Lee, Y. Z., Calderon-Colon, X., Sultana, S., Lu, J., and Zhou, O. (2010). Prospective-gated cardiac micro-CT imaging of free-breathing mice using carbon nanotube field emission x-ray. *Medical Physics*, 37(10):5306.

Cao, G., Lee, Y. Z., Liu, Z., Rajaram, R., Peng, R., Calderon-Colon, X., An, L., Wang, P., Phan, T., Lalush, D., Lu, J., and Zhou, O. (2008). Respiratory-gated micro-CT using a carbon nanotube based micro-focus field emission x-ray source. *Proceedings of SPIE*, 6913:691304–691304–11.

Cao, G., Lee, Y. Z., Peng, R., Liu, Z., Rajaram, R., Calderon-Colon, X., An, L., Wang, P., Phan, T., Sultana, S., Lalush, D. S., Lu, J. P., and Zhou, O. (2009). A dynamic micro-CT scanner based on a carbon nanotube field emission x-ray source. *Physics in Medicine and Biology*, 54(8):2323–2340.

Cheng, Y. and Zhou, O. (2003). Electron field emission from carbon nanotubes. *Comptes Rendus Physique*, 4(9):1021–1033.

Chtcheprov, P., Burk, L., Yuan, H., Inscoe, C., Ger, R., Hadsell, M., and Lu, J. (2014). Physiologically gated microbeam radiation using a field emission x-ray source array. *Medical Physics*, 41(8).

Desjardins, B. and Kazerooni, E. A. (2004). ECG-Gated Cardiac CT. *American Journal of Roentgenology*, 182(4):993–1010.

Dobbins, J. T. and Mcadams, H. P. (2009). Chest tomosynthesis : Technical principles and clinical update. *European Journal of Radiology*, 72:244–251.

Dobbins, J. T., McAdams, H. P., Godfrey, D. J., and Li, C. M. (2008a). Digital Tomosynthesis of the Chest. *Journal of Thoracic Imaging*, 23(2):86–92.

Dobbins, J. T., Mcadams, H. P., Sabol, J. M., Chakraborty, D. P., Kazerooni, E. A., Reddy, G. P., Vikgren, J., and Bath, M. (2016). Multi-Institutional Evaluation of Digital Tomosynthesis, Dual-Energy Radiography, and Conventional Chest Radiography for the Detection and Management of Pulmonary Nodules: Appendix E1. *Radiology*, 000(January):1998.

Dobbins, J. T., McAdams, H. P., Song, J.-W., Li, C. M., Godfrey, D. J., DeLong, D. M., Paik, S.-H., and Martinez-Jimenez, S. (2008b). Digital tomosynthesis of the chest for lung nodule detection: Interim sensitivity results from an ongoing NIH-sponsored trial. *Medical Physics*, 35(6):2554.

Dournes, G., Menut, F., Macey, J., Fayon, M., Chateil, J.-F., Salel, M., Corneloup, O., Montaudon, M., Berger, P., and Laurent, F. (2016). Lung morphology assessment of cystic fibrosis using MRI with ultra-short echo time at submillimeter spatial resolution. *European Radiology*, 26(11):3811–3820.

Gibson, R. L., Burns, J. L., and Ramsey, B. W. (2003). Pathophysiology and Management of Pulmonary Infections in Cystic Fibrosis. *American Journal of Respiratory and Critical Care Medicine*, 168(8):918–951.

Good, W. F., Abrams, G. S., Catullo, V. J., Chough, D. M., Ganott, M. A., Hakim, C. M., and Gur, D. (2008). Digital breast tomosynthesis: A pilot observer study. *American Journal of Roentgenology*, 190(4):865–869.

Håkansson, M., Båth, M., Börjesson, S., Kheddache, S., Flinck, A., Ullman, G., and Månsson, L. G. (2005). Nodule detection in digital chest radiography: Effect of nodule location. *Radiation Protection Dosimetry*, 114(1-3):92–96.

Hamanaka, M. H. M. O., Mammana, V. P., and Tatsch, P. J. (2013). Review of Field Emission from Carbon Nanotubes: Highlighting Measuring Energy Spread. *NanoCarbon 2011*, 3.

Iii, J. T. D. and Godfrey, D. J. (2003). Digital x-ray tomosynthesis : current state of the art. *Phys. Med. Biol*, 48(R):65–106.

Johnsson, Å. A., Vikgren, J., and Båth, M. (2014a). A Retrospective Study of Chest Tomosynthesis as a Tool for Optimizing the use of Computed Tomography Resources and Reducing Patient Radiation Exposure. *Academic Radiology*, 21(11):1427–1433.

Johnsson, A. A., Vikgren, J., and Bath, M. (2014b). Chest tomosynthesis: Technical and clinical perspectives. *Seminars in Respiratory and Critical Care Medicine*, 35:17–26.

Johnsson, A. . A., Vikgren, J., Svalkvist, A., Zachrisson, S., Flinck, A., Boijsen, M., Kheddache, S., Månsson, L. G., and Båth, M. (2010). Overview of two years of clinical experience of chest tomosynthesis at Sahlgrenska university hospital. *Radiation Protection Dosimetry*, 139(1-3):124–129.

Kandlakunta, P., Pham, R., Khan, R., and Zhang, T. (2017). Development of multi-pixel x-ray source using oxide coated cathodes. *Physics in Medicine and Biology*, 101(1-2):158–162.

Kwan, A. L. C., Boone, J. M., Yang, K., and Huang, S.-Y. (2007). Evaluation of the spatial resolution characteristics of a cone-beam breast CT scanner. *Medical Physics*, 34(1):275.

Langer, S. G., Graner, B. D., Schueler, B. a., Fetterly, K. a., Kofler, J. M., Mandrekar, J. N., and Bartholmai, B. J. (2016). Sensitivity of Thoracic Digital Tomosynthesis (DTS) for the Identification of Lung Nodules. *Journal of Digital Imaging*, 29(1):141–147.

Lell, M., Marwan, M., Schepis, T., Pflederer, T., Anders, K., Flohr, T., Allmendinger, T., Kalender, W., Ertel, D., Thierfelder, C., Kuettner, A., Ropers, D., Daniel, W. G., and Achenbach, S. (2009). Prospectively ECG-triggered high-pitch spiral acquisition for coronary CT angiography using dual source CT: Technique and initial experience. *European Radiology*, 19(11):2576–2583.

Lell, M. M., Scharf, M., Eller, A., Wuest, W., Allmendinger, T., Fuchs, F., Achenbach, S., Uder, M., and May, M. S. (2016). Feasibility of respiratory-gated high-pitch spiral CT: Free-breathing inspiratory image quality. *Academic Radiology*, 23(4):406–412.

Li, X., Samei, E., Segars, W. P., Sturgeon, G. M., Colsher, J. G., and Frush, D. P. (2008). Patient-specific dose estimation for pediatric chest CT. *Medical physics*, 35(12):5821–5828.

Meltzer, C., Båth, M., Kheddache, S., Ásgeirsdóttir, H., Gilljam, M., and Johnsson, Å. A. (2016). Visibility of structures of relevance for patients with cystic fibrosis in chest tomosynthesis: Influence of anatomical location and observer experience. *Radiation Protection Dosimetry*, 169(1-4):177–187.

Mott, L. S., Graniel, K. G., Park, J., De Klerk, N. H., Sly, P. D., Murray, C. P., Tiddens, H. a. W. M., and Stick, S. M. (2013). Assessment of early bronchiectasis in young children with cystic fibrosis is dependent on lung volume. *Chest*, 144(4):1193–1198.

Neculaes, V. B., Edic, P. M., Frontera, M., Caiafa, A., Ge Wang, and De Man, B. (2014a). Multisource X-Ray and CT: Lessons Learned and Future Outlook. *IEEE Access*, 2(c):1568–1585.

Neculaes, V. B., Edic, P. M., Frontera, M., Caiafa, A., Ge Wang, and De Man, B. (2014b). Multisource X-Ray and CT: Lessons Learned and Future Outlook. *IEEE Access*, 2(c):1568–1585.

Nicolaou, S., Eftekhari, A., Sedlic, T., Hou, D. J., Mudri, M. J., Aldrich, J., and Louis, L. (2008). The utilization of dual source CT in imaging of polytrauma. *European Journal of Radiology*, 68(3):398–408.

O'Connor, O. J., Vandeleur, M., McGarrigle, A. M., Moore, N., McWilliams, S. R., McSweeney, S. E., O'Neill, M., Ni Chroinin, M., and Maher, M. M. (2010). Development of low-dose protocols for thin-section CT assessment of cystic fibrosis in pediatric patients. *Radiology*, 257(3):820–829.

Oppelt, A. (2005). *Imaging systems for medical diagnostics*. John Wiley & Sons.

Petersilka, M., Bruder, H., Krauss, B., Stierstorfer, K., and Flohr, T. G. (2008). Technical principles of dual source CT. *European Journal of Radiology*, 68(3):362–368.

Pollock, S., Kipritidis, J., and Lee, D. (2016). The impact of breathing guidance and prospective gating during thoracic 4DCT imaging: an XCAT study utilizing lung cancer patient motion. *Physics in Medicine & Biology*, pages 6485–6501.

Prince, J. and Links, J. (2006). *Medical Imaging Signals and Systems*.

Qian, X., Tucker, A., Gidcumb, E., Shan, J., Yang, G., Calderon-Colon, X., Sultana, S., Lu, J., Zhou, O., Spronk, D., Sprenger, F., Zhang, Y., Kennedy, D., Farbizio, T., and Jing, Z. (2012). High resolution stationary digital breast tomosynthesis using distributed carbon nanotube x-ray source array. *Medical Physics*, 39(4):2090.

Quaia, E., Grisi, G., Baratella, E., Cuttin, R., Poillucci, G., Kus, S., and Cova, M. A. (2014). Diagnostic imaging costs before and after digital tomosynthesis implementation in patient management after detection of suspected thoracic lesions on chest radiography. *Insights into imaging*, 5(1):147–55.

Rasmussen, T., Køber, L., Abdulla, J., Pedersen, J. H., Wille, M. M. W., Dirksen, A., and Kofoed, K. F. (2015). Coronary artery calcification detected in lung cancer screening predicts cardiovascular death. *Scandinavian Cardiovascular Journal*, 49(3):159–167.

Sabol, J. M. (2009). A Monte Carlo estimation of effective dose in chest tomosynthesis. *Medical physics*, 36(12):5480–5487.

Saguintaah, M., Cabon, Y., Gauthier, R., Duboibaudry, C., Couderc, L., Le Bourgeois, M., Reix, P., Chiron, R., Arrada, I. T., Molinari, N., and Matecki, S. (2017). A simplified, semi-quantitative structural lung disease computed tomography outcome during quiet breathing in infants with cystic fibrosis. *Journal of Cystic Fibrosis*, 16(1):151–157.

Sechopoulos, I. (2013). A review of breast tomosynthesis. Part I. The image acquisition process. *Medical physics*, 40(1):014301.

Seibert, J. Anthony, Boone, J. M. (2005). X-Ray Imaging Physics for Nuclear Medicine Technologists. *Journal of Nuclear Medicine Technology*, 33(1):3–18.

Shan, J. (2015). *Development of a Stationary Chest Tomosynthesis System Using*. PhD thesis, University of North Carolina at Chapel Hill.

Shan, J., Burk, L., Wu, G., Lee, Y. Z., Heath, M. D., Wang, X., Foos, D., Lu, J., and Zhou, O. (2015a). Prospective gated chest tomosynthesis using CNT X-ray source array. In Hoeschen, C., Kontos, D., and Flohr, T. G., editors, *SPIE Medical Imaging: Physics of Medical Imaging*, volume 9412, page 941242.

Shan, J., Chtcheprov, P., Tucker, A. W., Lee, Y. Z., Wang, X., Foos, D., Heath, M. D., Lu, J., and Zhou, O. (2013). Stationary chest tomosynthesis using a CNT x-ray source array. *SPIE Medical Imaging: Physics of Medical Imaging*, 81.

Shan, J., Tucker, A. W., Gaalaas, L. R., Wu, G., Platin, E., Mol, A., Lu, J., and Zhou, O. (2015b). Stationary intraoral digital tomosynthesis using a carbon nanotube X-ray source array. *Dentomaxillofacial Radiology*, 44(9):1–9.

Shan, J., Tucker, A. W., Lee, Y. Z., Heath, M. D., Wang, X., Lu, J., Zhou, O., and Hill, C. (2014a). Evaluation of imaging geometry for stationary chest tomosynthesis. In Whiting, B. R. and Hoeschen, C., editors, *Proc. SPIE*, volume 9033, pages 903317–1.

Shan, J., Tucker, A. W., Lee, Y. Z., Lu, J., and Zhou, O. (2014b). Stationary chest tomosynthesis using a carbon nanotube x-ray source array : a feasibility study. *Physics in medicine and biology*, 60(1).

Sly, P. D., Gangell, C. L., Chen, L., Ware, R. S., Ranganathan, S., Mott, L. S., Murray, C. P., and Stick, S. M. (2013). Risk factors for bronchiectasis in children with cystic fibrosis. *The New England journal of medicine*, 368(21):1963–70.

Stern, M., Wiedemann, B., and Wenzlaff, P. (2008). From registry to quality management: the German Cystic Fibrosis Quality Assessment project 1995 2006. *European Respiratory Journal*, 31(1):29–35.

Terzi, A., Bertolaccini, L., Viti, A., and Comello, L. (2013a). Lung Cancer Detection with Digital Chest Tomosynthesis. *Journal of Thoracic Oncology*, 8(6):685–692.

Terzi, a., Bertolaccini, L., Viti, a., Comello, L., Ghirardo, D., Priotto, R., and Grosso, M. (2013b). Lung cancer detection with digital chest tomosynthesis: Baseline results from the observational study SOS. *Journal of Thoracic Oncology*, 8(6):685–692.

Tingberg, A. (2010). X-ray tomosynthesis: a review of its use for breast and chest imaging. *Radiation Protection Dosimetry*, 139(1-3):100–107.

Tomashefski, J. F., Bruce, M., Goldberg, H. I., and Dearborn, D. G. (1986). Regional Distribution of Macroscopic Lung Disease in Cystic Fibrosis 1 I-3. *American Review of Respiratory Disease*, 133:535–540.

Tucker, A. W., Calliste, J., Gidcumb, E. M., Wu, J., Kuzmiak, C. M., Hyun, N., Zeng, D., Lu, J., Zhou, O., and Lee, Y. Z. (2014). Comparison of a Stationary Digital Breast Tomosynthesis System to Magnified 2D Mammography Using Breast Tissue Specimens. *Academic Radiology*, 21(12):1547–1552.

Tucker, A. W., Kuzmiak, C. M., Inscoe, C., Lee, Y. Z., Lu, J., and Zhou, O. (2013). Feasibility of stationary digital breast tomosynthesis as an effective screening tool for patients with augmentation mammoplasty. *Medical Imaging 2013: Physics of Medical Imaging*, 8668:86685N.

Vikgren, J., Zachrisson, S., Svalkvist, A., Johnsson, A. a., Boijsen, M., Flinck, A., Kheddache, S., and Båth, M. (2008). Comparison of chest tomosynthesis and chest radiography for detection of pulmonary nodules: human observer study of clinical cases. *Radiology*, 249(3):1034–1041.

Von Steyern, K. V., Björkman-Burtscher, I. M., Höglund, P., Bozovic, G., Wiklund, M., and Geijer, M. (2012). Description and validation of a scoring system for tomosynthesis in pulmonary cystic fibrosis. *European Radiology*, 22:2718–2728.

Vult von Steyern, K., Björkman-Burtscher, I., and Geijer, M. (2012). Tomosynthesis in pulmonary cystic fibrosis with comparison to radiography and computed tomography: A pictorial review.

Wu, G., Inscoe, C., Calliste, J., Lee, Y. Z., Zhou, O., Lu, J., Carolina, N., and Hill, C. (2015). Adapted fan-beam volume reconstruction for stationary digital breast tomosynthesis. *Proc. SPIE*, 9412:1–10.

Yamada, Y., Jinzaki, M., Hasegawa, I., Shiomi, E., Sugiura, H., Abe, T., Sato, Y., Kuribayashi, S., and Ogawa, K. (2011). Fast scanning tomosynthesis for the detection of pulmonary nodules: diagnostic performance compared with chest radiography, using multidetector-row computed tomography as the reference. *Investigative radiology*, 46(8):471–477.

Zhang, L., Yuan, H., Burk, L. M., Inscoe, C. R., Hadsell, M. J., Chtcheprov, P., Lee, Y. Z., Lu, J., Chang, S., and Zhou, O. (2014). Image-guided microbeam irradiation to brain tumour bearing mice using a carbon nanotube x-ray source array. *Physics in Medicine and Biology*, 59(5):1283–1303.

Zhou, O. Z. and Calderon-Colon, X. (2010). Carbon Nanotube-Based Field Emission X-ray Technology. In *Carbon Nanotube and Related Field Emitters: Fundamentals and Applications*, pages 417–440.